8-7-2024

Major and Trace Element Analysis of Irazú Volcano's Upper Holocene Magmatic Evolution, Costa Rica

Forrest Dabbs

Recommended Citation

Dabbs, Forrest, "Major and Trace Element Analysis of Irazú Volcano's Upper Holocene Magmatic Evolution, Costa Rica." Thesis, Georgia State University, 2024.
doi: https://doi.org/10.57709/37430278

Major and Trace Element Analysis of Irazú Volcano's Upper Holocene Magmatic Evolution, Costa Rica

by

Forrest E. Dabbs

Under the Direction of Paulo J. Hidalgo, PhD

A Thesis Submitted in Partial Fulfillment of the Requirements for the Degree of

Master of Science

in the College of Arts and Sciences

Georgia State University

2024

ABSTRACT

The Irazú Volcano is an active andesitic shield volcano located ~15 kilometers northeast of Costa Rica's second-largest city, Cartago. Tephra deposits from the past 2600 years confirm that Irazú's history is punctuated with phreatomagmatic, magmatic, and phreatic eruptions that produced ashfall, pyroclastic flows, and lahars. However, geological studies have concentrated on the 1963-1965 eruptions and lack a geochemical assessment of Irazú's 2,400 years of activity. Employing inductively coupled plasma mass spectrometry (ICP-MS) and x-ray fluorescence (XRF), major and trace elements of ash and whole-rock tephra deposits are correlated with Irazú's stratigraphy to provide a geochemical characterization, model Irazú's magmatic evolution, and ascertain eruptive trends. The high-resolution magmatic trends measured in this project are directly linked to the magma's viscosity and mineral content. This work defines a geochemical approach to hazard mapping that could benefit 60% of the nation's population.

INDEX WORDS: Irazú volcano, Tephrochronology, Geochemistry, Volcanology, Petrology

Major and Trace Element Analysis of Irazú Volcano’s Upper Holocene Magmatic Evolution, Costa Rica

by

Forrest E. Dabbs

Committee Chair: Paulo Hidalgo

Committee: Hassan Babaie

Brian Meyer

Electronic Version Approved:

Office of Graduate Services

College of Arts and Sciences

Georgia State University

August 2024

DEDICATION

To my husband, Olyn, our angel Nora, and Smolcat.

ACKNOWLEDGEMENTS

This endeavor would not have been possible without my thesis advisor and professor, Dr. Paulo Hidalgo. I am grateful for the years of mentorship. I would like to express my deepest gratitude to my classmates Magnolia McLaughlin and Kiersten Crye, for their sense of humor and support. Special thanks to Dr. Alvarado Guillermo, Dr. Daniela Campo-Durian, and Dr. Peter Ryan for their collaboration and expertise. I would be remiss in not mentioning the National Science Foundation for partially supporting this project through award 2106712, the 2021 Graduate Research Assistantship.

TABLE OF CONTENTS

LIST OF TABLES

LIST OF FIGURES

LIST OF ABBREVIATIONS

Al_2O_3 – Aluminum Oxide

BCE – Before Current Era

CaO – Calcium Oxide

CAVF – Central American Volcanic Front

CIPW – Cross, Iddings, Pirsson, and Washington; normative mineralogy calculation

CCRDB - Central Costa Rican Deformation Belt

CE – Before Current Era

ECC – Eastern Cinder Cones

Fe_2O_3 – Iron (III) Oxide

GMA - Greater Metropolitan Area

HNO_3 – Nitric Acid

IAB – Island Arc Basalt

ICP-MS – Inductively Coupled Plasma Mass Spectrometry

K_2O – Potassium Oxide

KED – Kinetic Energy Discrimination

LOI – Loss-On-Ignition

MAT – Middle American Trench

MgO – Magnesium Oxide

MORB – Mid-Ocean Ridge Basalt

Na_2O – Sodium Oxide

NH_4NO_3 – Ammonium Nitrate

OIB – Ocean Island Basalt

PDC – Pyroclastic Density Current

REE – Rare Earth Elements

SiO_2 – Silicon Dioxide

SSC – Southern Scoria Cones

TAS – Total Alkali Silica

USGS – United States Geological Survey

VEI – Volcanic Explosivity Index

XRF – X-ray Fluorescence

VAF – Volcanic Arc Fault

1 INTRODUCTION

This document presents a detailed geochemical analysis and trace element correlation of the Irazú volcano Upper Holocene tephras, with guidance from recent stratigraphy and radiocarbon dating by Campos et al. (2024), to chemically characterize Irazú's eruptive trends over the last 2,400 years. This analysis allows for the identification of patterns, such as shifts in magma composition or variations in eruption styles, which are vital for eruption forecast and their potential impacts. Moreover, understanding the geochemical evolution of Irazú Volcano provides invaluable information for hazard assessment and mitigation strategies, aiding in protecting nearby communities and infrastructure against volcanic threats.

1.1 Tectonic and geologic setting

At the southeastern end of the 1,200 km long (Goss et. al., 2006) Central American Volcanic Front (CAVF) in the Cordillera Central lies the basaltic-andesite shield volcano, Irazú. Costa Rica's Irazú volcano stands at 3,432m and has a volume of ~600 km3, making it the country's tallest and largest volcanic edifice (Alvarado & Schmincke, 2013). The volcano is 24 km east of the capital, San José, and 15 km northwest of the country's second-largest city, Cartago.

Irazú's tectonic history is as active as the volcano itself. Along the Middle American Trench (MAT), the Cocos plate (~23 Ma) obliquely subducts N23E under the Caribbean plate at a rate of ~88 mm/yr (DeMets 2011, Arroyo et. al., 2020). It is the sum of a smooth upper region and a southern area of rougher seamounts (Hayes et, al., 2013). It's the convergence of these opposing topographic areas, observed in Figure 1.2, that has produced the seismically active Central Costa Rican Deformation Belt (Arroyo et. al., 2020) and the calc-alkaline Central

American Volcanic Front (Goss et. al., 2006). Clustered at the tail end of this volcanic forearc lay the Irazú-Turrialba Volcanic complex, Poas Volcano (active), and the dormant Barva Volcano.

Irazú volcano is built upon a Pliocene volcanic basement (Campos et.al., 2024) and is characterized by its intricate summit structures. The 700 m wide, active Main Crater, which is distinguished by its frequent fumarole activity and relics of the 1963 eruptions, sits to the west of the Diego de la Haya Crater, last active in 1723 (Murata et al., 1966, Pavanelli et. al., 2004). These two craters rest in the ancient Playa Hermosa Caldera, which has a diameter of 1200 m (Pérez-Umaña et. al., 2019) and is referred to by Alvarado (2011) as Irazú's debut. The structures of the volcanic edifice include several active faults with primary orientations of NW-SE and E-W, as mapped by Campos and others (2024). Alvarado (1993, 2006) identifies a string of prehistoric cinder cones on the E-W summit and southern flank and two tuff rings southeast of the crater.

Based on the 3-D density models calculated by Lücke and Arroyo, (2015), the Cocos Plate beneath the Irazú crater extends ~110 km. Seismological studies by Montero (1989), Montero and Alvarado (1995) and geodetic data produced by Murata et al., (1966) and Alvarado et al., (2006) suggest the presence of two small, shallow magma chambers ~0.6–1.8 km and 3.2–4 km beneath the summit.

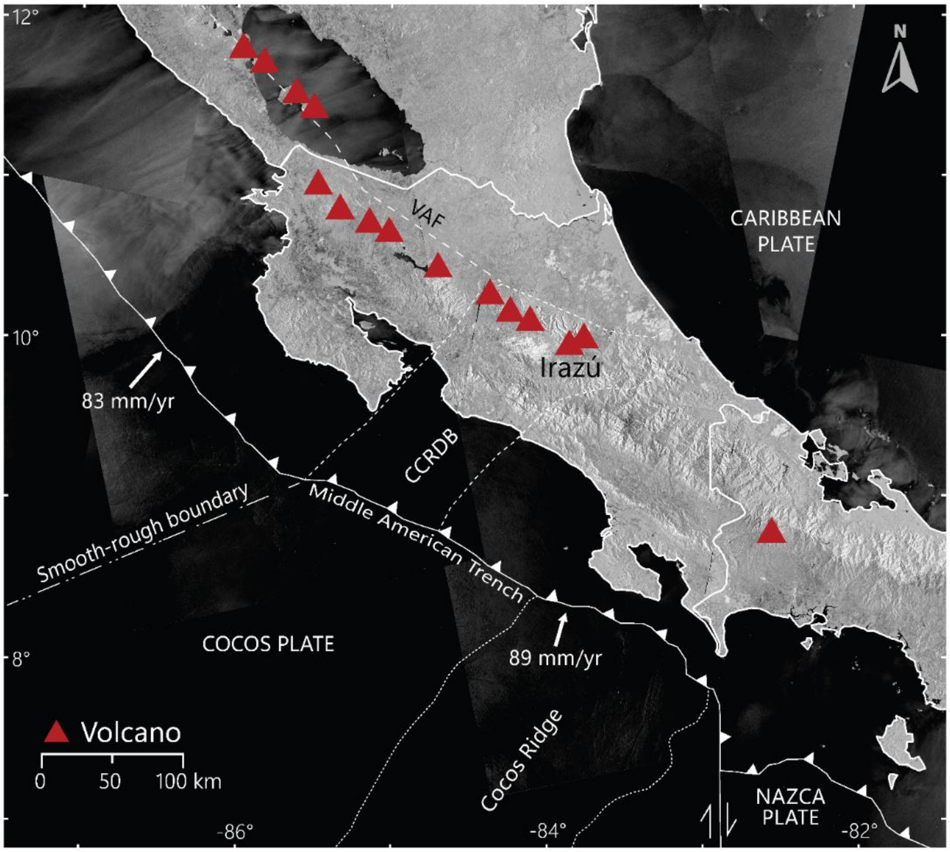

Figure 1: The Cocos Plate obliquely subducts eastward along the Middle American Trench and under the Caribbean plate. Irazú volcano is situated within the Central Costa Rican Deformation Belt (CCRDB), at the southern end of the Volcanic Arc Fault (VAF). The tectonic map is adapted from Arroyo et. al., 2020.

1.2 Problem statement and importance

Surrounding the active Irazú volcano is the densely populated Greater Metropolitan Area (GMA). According to The Nature Conservancy (2024), 2.6 million residents, or ~60% of Costa Rica's population, reside in this urbanized area that includes San José, Alajuela, Cartago, and Heredia.

Between 1723 and 1965, Irazú experienced several eruptions varying from a Volcanic Explosivity Index (VEI) of 1 to 3 (Alvarado, 1993 and Campos-Duran et. al., 2024). These eruption periods varied from several hours to months, or even years. This seemingly sporadic and complex eruptive behavior is just one of the many reasons why the Irazú volcano is one of the most studied in Central America, with previous investigations providing valuable geological, petrological, stratigraphic, geochronological, tephrostratigraphical, and chemical data (Alvarado et. al., 2006; Alvarado & Schmincke, 2013; Alvarado, 1993; Clark et al., 1998, 2006; Campos et. al., 2024; Murata et al., 1966; Pavanelli et. al., 2004; Pérez-Umaña et. al., 2019).

Irazú's most recent (1963-1965) eruption reached a Volcanic Explosivity Index (VEI) of 3 and resulted in daily ashfall over the GMA. Lemieux's (1977) volcanic hazard research of the 1963-65 ashfalls describes the effects of the prolonged ashfall, which unfortunately was carried by prominent westerly winds from the summit to areas beyond San José, devastating physical and cultural environments, agriculture, wildlife, infrastructure, and public health.

This volcanic eruption resulted in sustained damage to nearly 75% of Costa Rica's economic production (Astorga, 2008) amounting to a loss of $12,000,000 (Murata et al., 1966). The eruption resulted in the loss of crops, coffee, potatoes, corn, tobacco, and tomatoes, livestock health issues, infrastructure damage (communications, public utilities, and housing), local businesses, tourism, and commercial activities (Lemieux, 1977). During this time, San José, the capital city located 30 km from the volcano, was referred to as the "city of brooms" (Armbrister, 1964) due to the daily ash deposits, which reached at least 1 g/cm² during the peak activity (Castillo et, al., 2018). The accumulation of ash on the ground triggered debris flows, resulting in the deaths of 20 people and the destruction of approximately 300 houses (Waldron, 1967). Although Irazú is presently less active, ongoing hazards affect the surrounding cities. Previous hazard studies by Waldron (1967), Ulate and others (1966), Pavanelli (2004), and Castillo et. al., (2018) investigate ash fallout, debris flow, erosion control, mudflow, and flank instability.

Within a 6 km radius of the Irazú summit, 19 tephra units spanning the last 2.6 thousand years have been identified (Alvarado, 2006; Clark et. al., 1998, 2006; Campos et. al., 2024, Alvarado, 1993). However, despite the breadth of research conducted on Irazú, a high-resolution geochemical analysis of its eruptive history remains elusive with available data being temporarily constrained to the strombolian eruption of 1723 and the most recent volcanic eruption from 1963 to 1965.

The reach of this study is exemplified by our international and local partnerships with the National Risk Prevention Commission and Emergency Care (CNE) of Costa Rica, the Costa Rican National Park Service, the local ASADA (Community Water Management Association), and the University of Barcelona School of Geographic Sciences.

The geochemical data, organized by their stratigraphic positions, revealed highly mafic pulses around 700 and 900 CE, each followed by a period of MgO depletion. Separate subgroups from the SSC and ECC cinder cones, although 1500 years apart, shared similar major compositions. Most samples exhibited K_2O and SiO_2 values indicative of high-potassium calc-alkaline magma series. Trace and REE ratios, sensitive to chemical fractionation, provided insights into Irazú’s geochemical history, source characteristics, partial melting degree and type, and fractional crystallization and contamination processes. Lanthanum to Samarium (La/Sm) ratios suggested enrichment in light REEs, likely indicating partial melting processes. Lanthanum/Niobium (La/Nb) ratios distinguish tectonic settings, with higher ratios indicating a subduction-related source. Zr/Nb and Y/Nb ratios identified magma source characteristics, with higher ratios suggesting evolved magma or crustal contamination. High Ba/Nb ratios indicated a subduction zone environment, while the broad range of Ba/Nb ratios in Irazú samples reflected its complex tectonic history. Moderate Ba/Rb, Ba/Th, and Ba/La ratios suggested a mantle source with less extensive fractionation, consistent with alkaline basalts and subduction slab fluid presence.

The composition of tephra is a pivotal factor in understanding the wide-ranging hazards associated with volcanic eruptions. Our results could contribute to building effective disaster preparedness and response systems and generate local educational programs regarding Irazú's volcanic activity.

1.3 Research questions and objective

The two imparting research questions that serve as the basis of this research are:

1. What are the major, trace, and rare earth element (REE) characteristics of Irazú's tephras over the last 2400 years?
2. How do these chemical characteristics correlate with Irazú's modern history and eruption dynamics?

This document provides an in-depth geochemical analysis and trace element correlation of the Upper Holocene tephras from the Irazú volcano, guided by recent stratigraphy and radiocarbon dating by Campos et al. (2024). The goal is to chemically characterize Irazú's eruptive trends. This analysis helps identify patterns such as changes in magma composition or variations in eruption styles, which are crucial for eruption forecasting and understanding their potential impacts. Additionally, comprehending the geochemical evolution of Irazú Volcano offers essential insights for hazard assessment and mitigation strategies, aiding in the protection of nearby communities and infrastructure against volcanic threats.

1.4 Literature Review

Previous research offers valuable data and reports on the stratigraphic sequence, petrology, and long-term hazards assessment of Irazú (Alvarado, 2011; Alvarado et al., 2006, 2020; Alvarado and Schmincke, 2013; Alvarado, 1993; Campos-Durán et. al., 2024; Clark et. al., 1994, 1998, 2006; Murata et al., 1966) and understanding the magmatic processes driving Irazú and the implications for the broader Central American Volcanic Belt (Boyce and Hervig, 2009; Benjamin et. al., 2007, Clark et al., 1998, Epiard et. al., 2017; Oeser et. al., 2018).

Sieber and others (2013) catalog eruptions: 1994, 1977, 1963–65, 1939–40, 1933, 1930, 1928, 1924, 1917–21, 1885–86, 1875 ± 5, 1864, 1847, 1842, 1822–23, 1775?, 1726, 1723–24 and 1560 ± 75). Most of these volcanic events were characterized as low-explosive to medium-explosive eruptions (≤VEI 3) and long sustained periods of fumarolic exhalation activity (Rouwet et. al., 2021). Most relevant to this study are the reports produced by Alvarado and Schmincke (2013), Campos-Durán (2024), and Clark (2006) that focus on understanding Irazú's Upper Holocene volcanic activity (Table 1.5). Although these studies span various disciplines, they are constrained to prominent eruptive events and lack a geochemical analysis over the past 1,200 years.

Work by Alvarado et. al., 2006; Benjamin et. al., 2007; Boyce and Hervig, 2009; Clark et. al., 1998; Alvarado, 1993; and Ulloa et. al., 2018 characterized the volatile and mineral content of the most prominent eruptions, 1723 and 1963-1965.

Table 1: Irazú's eruptive history over the last 300 years
Dominant eruptive behavior of notable eruptions between 1723 and 1963-1965. The table is adapted from Campos-Duran, et al., (2024).

Year	Type of eruption	Duration	Maximum height of eruptive column above crater level (km)	VEI (max.)	Hazards
1723-1724	Strombolian, phreatomagmatic, and phreatic	≥ 12 months	> 2 km	3	Fallout, ballistic, PDCs, lahars, and seismicity.
1917-1921	Phreatomagmatic	≥ 44 months	~5.5	2	Fallout and PDCs.
1924	Phreatomagmatic	~2 months	¿?	~1	Fallout
1928-1930	Phreatomagmatic	~6.5 months	> 2 km	2	Fallout and lahars
1933	Phreatomagmatic	4 months	~5.5?	2	Fallout
1939-1940	Phreatomagmatic	9 months	~4.5	2	Fallout
1963 - 1965	Phreatomagmatic	30 months	8	3	Fallout, ballistic, PDC, and lahars

1.5 Thesis Structure

This thesis is organized into four sections. These include 1) the Introduction, which presents the area of study, research questions, objective, previous work, and implications of findings; 2) the Methodology including fieldwork and lab preparation; 3) XRF and ICP-MS Analysis and a geologic description of results, and 4) the Discussion that will focus on the correlation between the observed chemistry and explosivity, limitations of the study, and conclusions.

2 METHODS

Fieldwork, conducted in December of 2021, involved collecting 127 samples within 5.5 km of the Irazú Main Crater for geochemical analysis. To avoid cross-contamination, samples were collected from bottom to top. Outcrops were mapped based on the previously published stratigraphic columns by Campos-Duran and others (2024). Additionally, five samples were collected in reserve for future radiometric dating. Based on the extent of exposed tephras and/or rate of weathering, some outcrops did not yield as many samples as others. The tephra samples collected for this study have been divided into three subgroups: main crater samples, eastern cinder cones (ECC) samples, and southern scoria cone samples (SSC). Samples of the main crater and SSC lie in the south and southwest of the Irazú Main Crater, while the ECC samples lie immediately eastward of the secondary crater, Diego de la Haya.

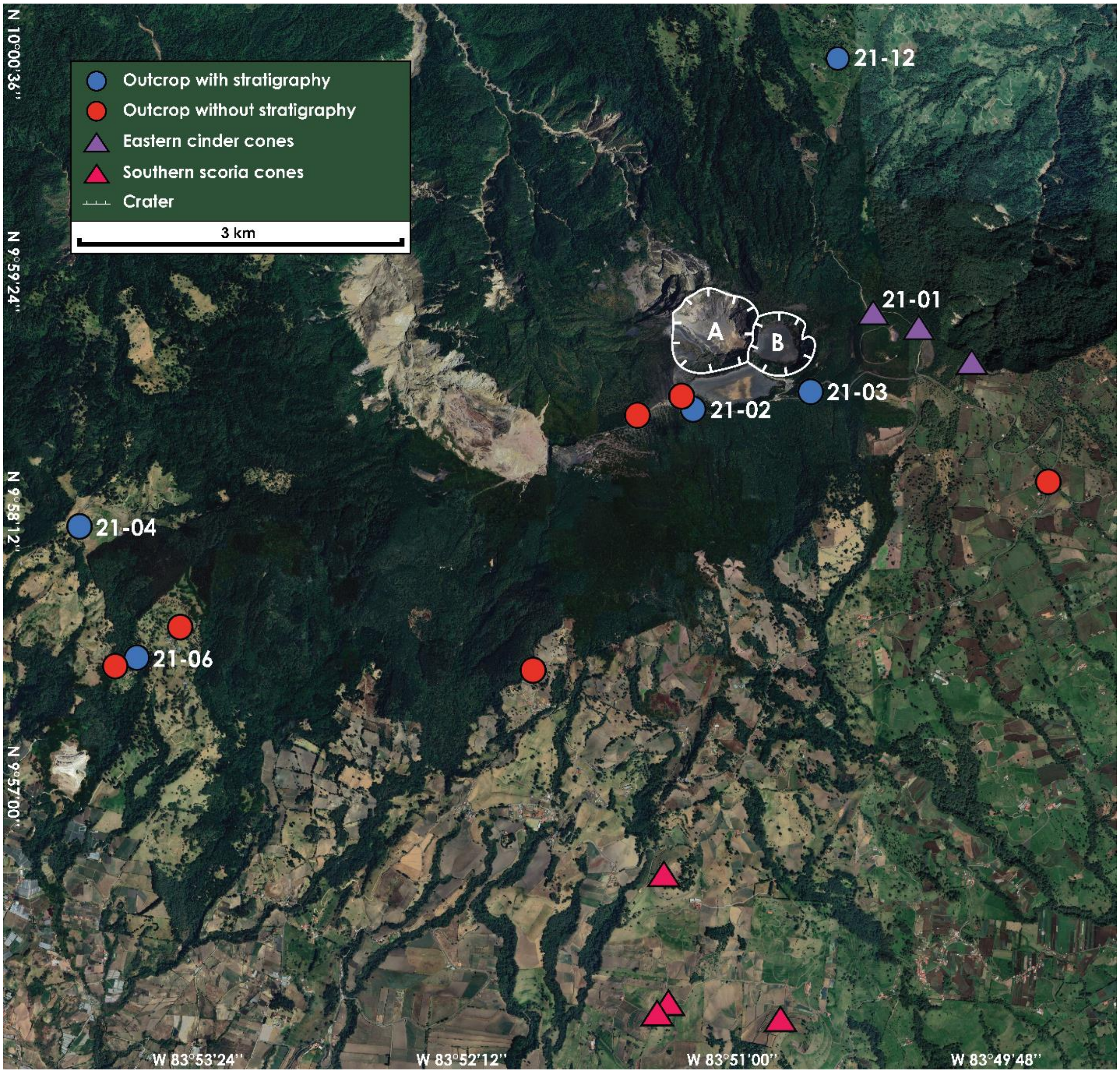

Figure 2: Sample locations are categorized into scoria cones directly south of the Main Crater (A), cinder cones east of crater Diego de la Haya (B) crater, samples with stratigraphy (labeled by column number), and without published stratigraphy. Satellite image used as the base map from Google Earth Pro.

2.1 Sample description overview

The tephra samples varied greatly in color, size, and maturity from one outcrop to another. This included red juvenile blocks, red and black scoria lapilli, fine to coarse-grained ash ranging from light to dark gray, and laminated massive ash beds with and without clasts.

The samples were collected within a 5.5 km radius of the crater, along Irazú's southeastern flank, and from within the two notable clusters of scoria cones referred to as the southern scoria cones (SSC) and the eastern cinder cones (ECC), seen in Figure 2. Over 50% of samples were collected within 1.7 km of the crater. The tephra layers most suitable for sampling were often found adjacent to paleosols and/or tephra layers exhibiting a high degree of hydrothermal alteration.

2.2 Sample collection and transportation

The 127 geochemical samples were collected in zipped plastic bags and transported to Georgia State University, Department of Geosciences in Atlanta, Georgia. The samples collected for future radiocarbon dating were packaged in aluminum foil and stored in Georgia State's petrology lab for future study.

2.3 Lab Methods

2.3.1 Sample preparation

The tephra samples were dried and held in a convection oven until ready for preparation. The LOI method applied here required samples to be held at 1000°C for two hours to remove organic material widely found welded within coarse-grained lapilli. The post-LOI samples were pulverized into a fine rock flour using an agate ball mill pulverizer for XRF and ICP-MS (major and trace) analysis.

2.4 X-ray Fluorescence (XRF) Analysis

2.4.1 Sample Preparation for XRF

The samples were prepared for XRF analysis by first weighing out 9.0000 (± 0.0005) grams of Claisse lithium tetraborate flux (66.67% lithium tetraborate with 32.83% lithium metaborate and 0.50% lithium iodide), 1.0000 (± 0.0005) gram of post-LOI sample powder, and 0.5000 gram of a wetting agent NH4NO3 using a Mettler PM240 Delta Range. The resulting mixture is a 9:1 fluxing agent-to-sample ratio. Samples were then fused in a Thermolyne 1300 furnace at 1100°C for 25 minutes, gently stirred, and poured into a preheated mold, held at 700°C. The mold was then transferred to a hot plate initially set to 500°C and cooled incrementally to 350°C.

2.4.2 XRF analysis

Each fused glass disk was inspected, weighed, labeled, and individually packaged for transport to Middlebury College in Vermont for evaluation using the Thermo Fisher Scientific ARL QUANTX EDXRF analyzer. Precision and accuracy of XRF analyses were quantified by replicate analyses of the following certified standards: BHVO-1, W-2, 278, BHVO-2, DNC-1,

QLO-1, RGM-1, AMH-1, STM-2, GSP-2, BIR-1, BCR-2, KPT-1, G-3. Over the range of concentrations for the elements examined in this study, precision is as follows: SiO_2 (±1.0%, e.g., 58.0 ± 0.58%); Al_2O_3 (±3.0%, e.g. 15.0 ± 0.45%); Fe_2O_3 (±3.0%, e.g. 10.0 ± 0.30%); MgO and CaO (±3.0%, e.g. 8.0 ± 0.24%); Na_2O (±5.0%, e.g. 3.0 ± 0.15%). The precision of K_2O analyses at low concentrations (<0.30 wt. %) found in these mafic powders is poor (e.g. ±20% of reported value), and K quantification is not a significant factor in the data analysis presented in this study.

2.5 Inductively Coupled Plasma-Mass Spectrometry (ICP-MS)

2.5.1 Preparation for ICP-MS

The fused glass discs previously used for XRF analysis were crushed into a fine rock powder using a Spex SamplePrep 8515 Shatterbox. Meanwhile, 20% and 5% HNO_3 stock solutions were prepared.

2.5.2 Acid Digestion

To complete the acid digestion of the powdered samples, 2.0000 (± 0.005) grams of rock flour and 50 mL of 20% nitric acid solution were combined into a 200 mL beaker, at a 1:100 ratio. After adding a pill magnet, the beaker was transferred to a stirring hotplate until the powdered sample was completely dissolved. The digested mixture was then diluted by adding 50 mL of 5% nitric acid. This 100x sample stock solution was labeled and stored in a sealed plastic jar until analysis. Prior to ICP-MS analysis, 5.00 mL of this solution plus 1.0 mL of internal standard (103Rh, 115I, 209Bi) solution was diluted to 100.0 mL with 5% HNO3. This was analyzed for trace element geochemistry.

2.5.3 ICP-MS Analysis

Trace element geochemistry was determined using a Thermo Fisher iCAP-Q quadrupole mass spectrometer operating in kinetic energy discrimination (KED) mode at Middlebury College in Vermont. Drift was quantified by (1) monitoring intensities of internal standards (103Rh, 115I, 209Bi) pipetted into samples, and (2) analyzing inline the USGS standards RGM-1 and/or BCR-2 every 5 samples. The ICP-MS results were corrected for samples with intensities within 80-125% of initial calibration. After the first sample tray was analyzed, it was noted that the intensities of the internal standards had declined to almost 80%. To address this, the ICP-MS autosampler rinse was increased from 2.5% nitric acid to 5% and the rinse time was also increased from 60 seconds to 90 seconds, resulting in better stability.

3 RESULTS

The chemical results and stratigraphic correlations are presented here in order from oldest to youngest, with emphasis on layers from known eruptive events and units identified by Clark and others (1998, 2006), Alvarado (1999), and Campos-Duran et. al. (2024). The results have been organized to delineate the temporal trends in eruptive activity and interpret the associated volcanic hazards affecting the GMA.

3.1 Stratigraphic Context

The sample areas are based on the fieldwork and stratigraphic columns completed by Clark (1993) and Campos-Duran et. al., (2024), which established fourteen detailed stratigraphic columns inaccessible areas within 6 km of Irazú, primarily on its NE and SW flanks, and transferred field data to a digital database built on a DEM created from aerial photographs taken between 2005 and 2007. Correlation between outcrops was achieved using volcanic-stratigraphic criteria and comparing lithological and sedimentological characteristics and integrated new stratigraphic sections with existing ones from Clark (1993). Campos-Duran and others (2024) utilized a distinctive and continuous tephra layer from the nearby Turrialba volcano as a marker horizon to refine stratigraphic correlation. By incorporating radiocarbon data and historical records, the study established the tephrostratigraphy of Irazú's uppermost part, preserving the original stratigraphic nomenclature and adding new layers with numerical designations. To maintain continuity between studies the outcrops will be referred to by their designations as published.

Table 2: Summary of stratigraphy

Relative age of each column based on the fieldwork and stratigraphy by Campos-Duran and others (2024). Column identifications are preserved from this work to maintain continuity.

Column ID	Coordinates	Elevation (m)	Sampled Unit	Site Description	Age (CE.)
-	9.942898 -83.854387	3009	SSC	~4.2-5.0 km SW of the crater	6024-5912
21-04	9.968011 -83.89859	2930	E1, E2, E4, E5	Road outcrop at Cabeza de Vaca Farm	~300 BCE -600
21-06	9.958514 -83.894249	2725	D1, A4, A1	Road cut 5.64 km S43W of the crater	~300 BCE -1965
21-03	9.977185 -83.843426	3358	D1, A4, A1	50 m W of the Irazú Volcano National Park entrance	~700-1965
21-02	9.975774 -83.852203	3402	C2, A4	~250 m E of the San Gerardo farm	~1300-1965
21-01 No illustration	9.982451 -83.834988	3232	ECC	Cono la Laguna	~1480-1640
21-12 No illustration	9.977185 -83.839793	5277		3.1 km N24E of the crater	~300 BCE -1965
21-10	9.976725 -83.853055	3425	A4	0.7 km S56W of the crater	~1300-1965

Owing to the sporadic exposures, rate of weathering, and extent of vegetation there lacks a continuum amongst layers across the stratigraphic columns. As a result, not every tephra layer has been identified and correlated to each column. This is most apparent by the comparison of columns 12-03 and 12-04 below. The following illustrated stratigraphic columns have been adapted from the work of Campos-Duran and others (2024).

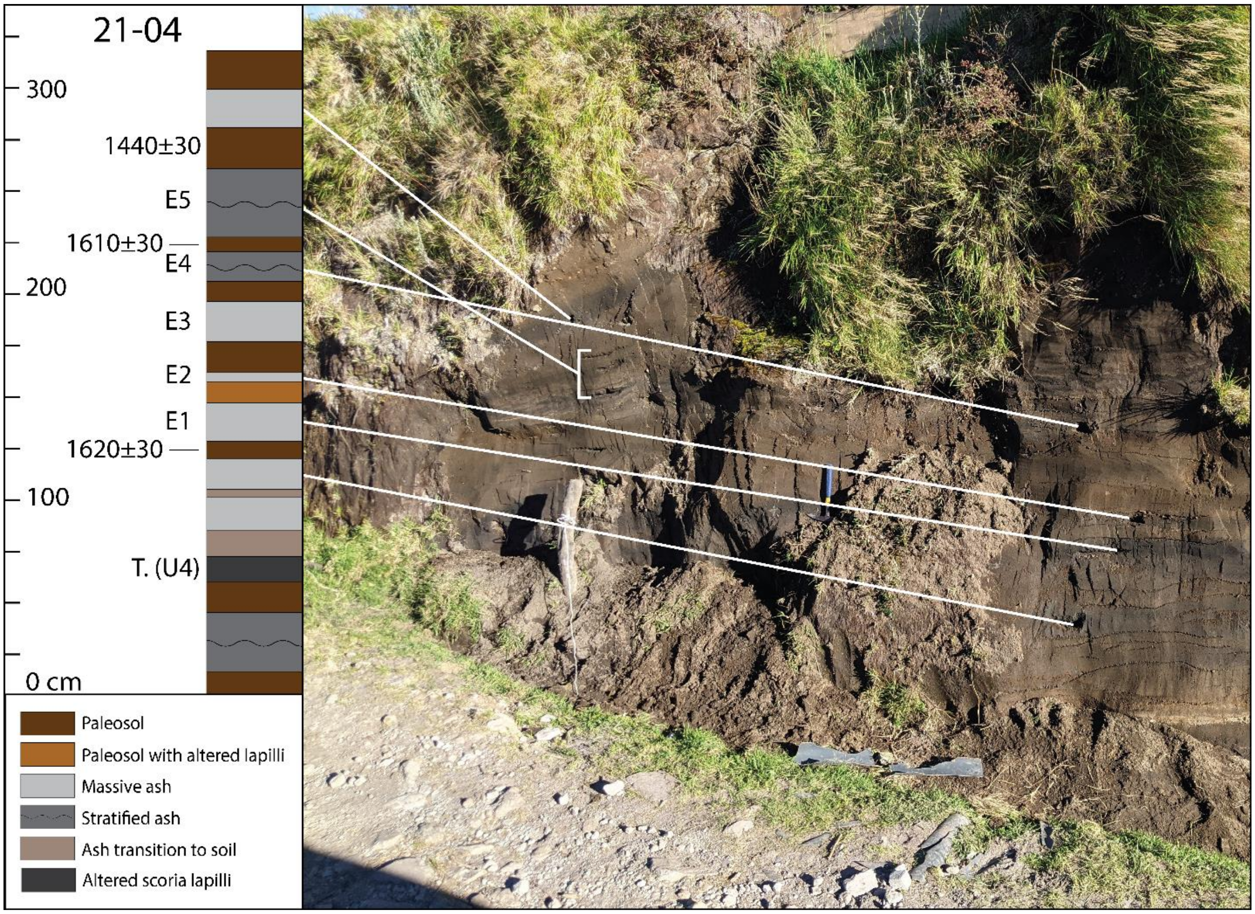

Figure 2: Stratigraphic column 12-04 displays the carbon-14 dates of paleosol layers to the left, indicating an age range of ~200 years. Unit T. (U4) was deposited by the neighboring Turrialba Volcano around 25 CE

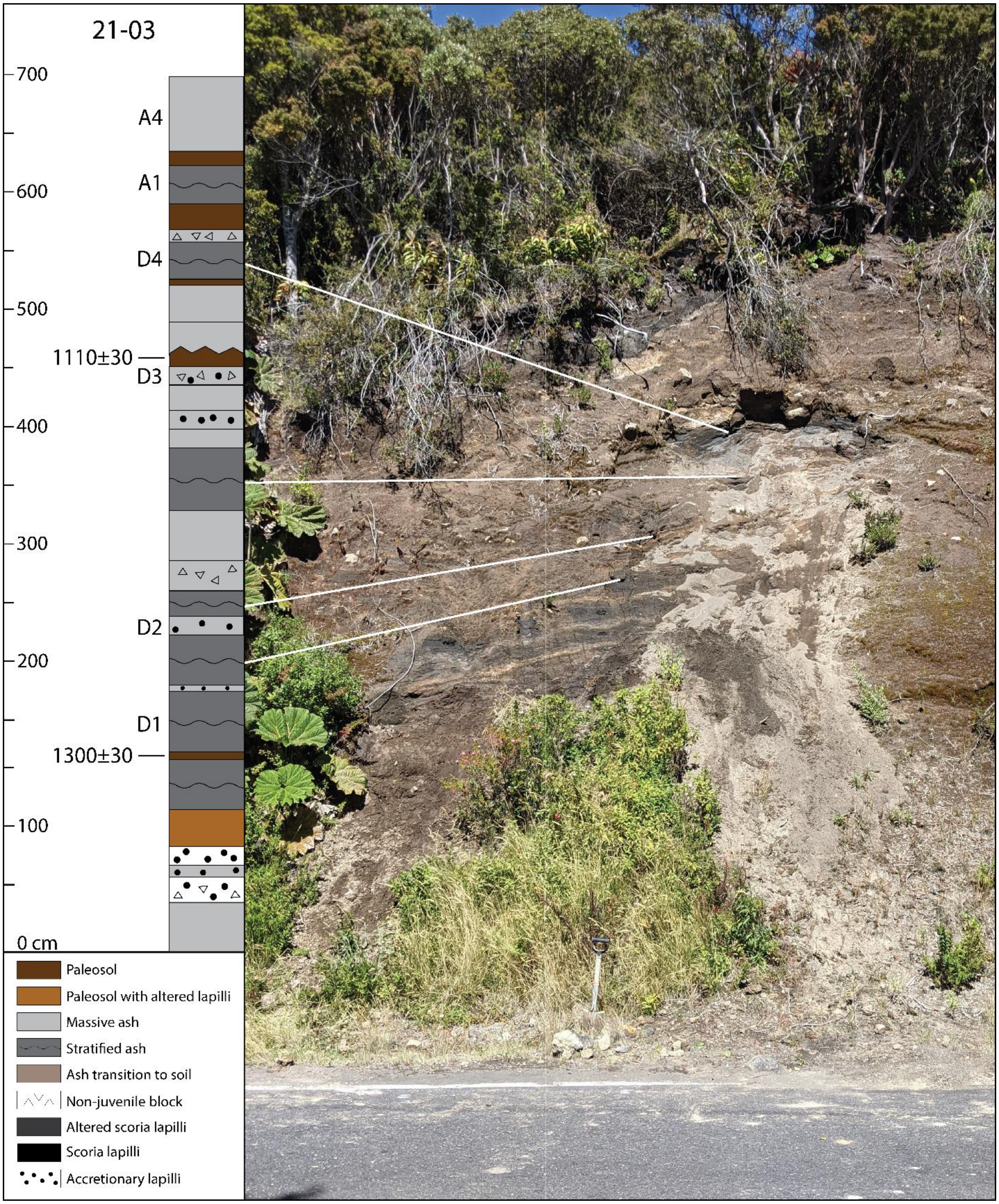

Figure 3: Stratigraphic column 12-03 contains carbon-14 dated paleosol layers 1300±30 yr. B.P. (~720 CE) and 1100±30 yr. B.P. (~720 CE), unit D1 (~700 CE), D2 (~800 CE), D3 (~850 CE), D4 (~1000 CE), unit A1 (1723 CE), and A4 (1963-1965 CE)(Campos-Duran et. al., 2024).

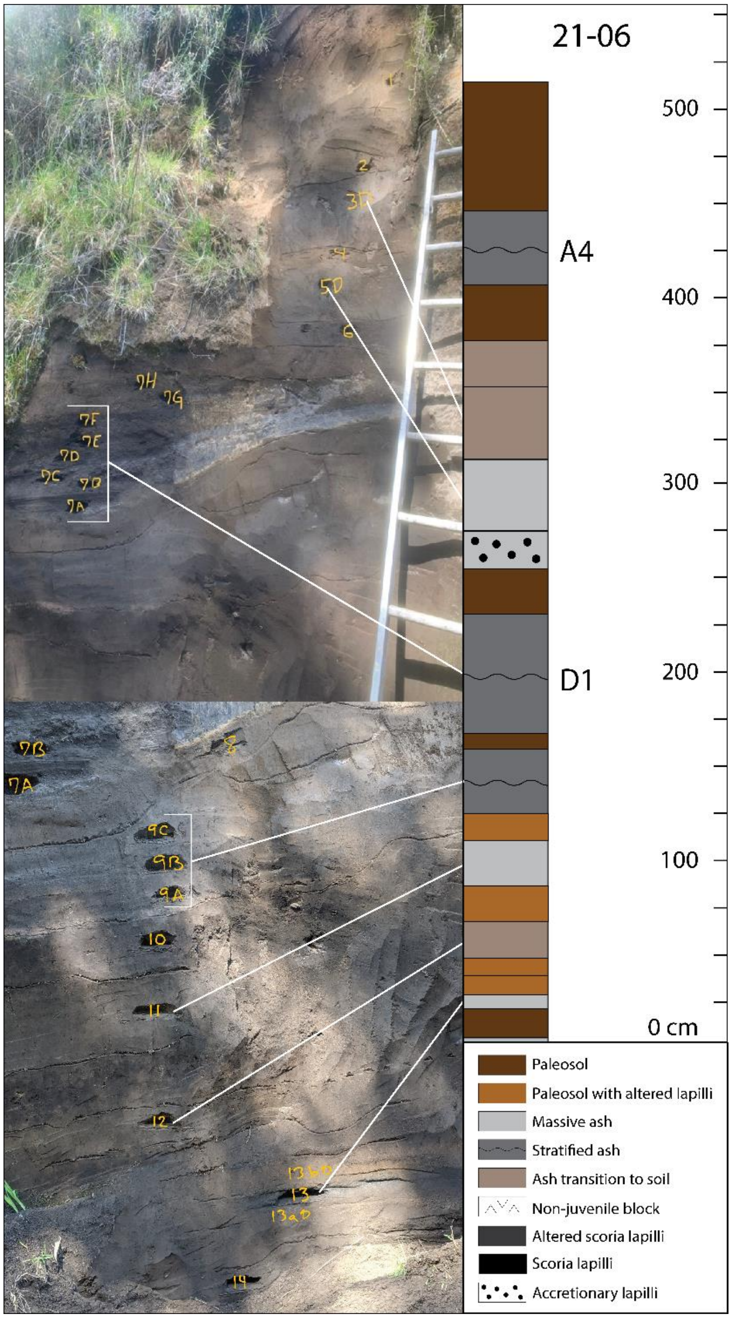

Figure 4: The key units of column 12-06 are D1 (~700 CE) and A4 from the recent 1963-1965 eruption (VEI 3).

Figure 5: Column 12-02 includes unit C1 (relative age of ~1300 CE), unit C2 (age of ~1420 CE, a paleosol layer dated 510±30 yr. B.P. (calibrated age ~1510 CE), and unit A4 (1963-1965 CE).

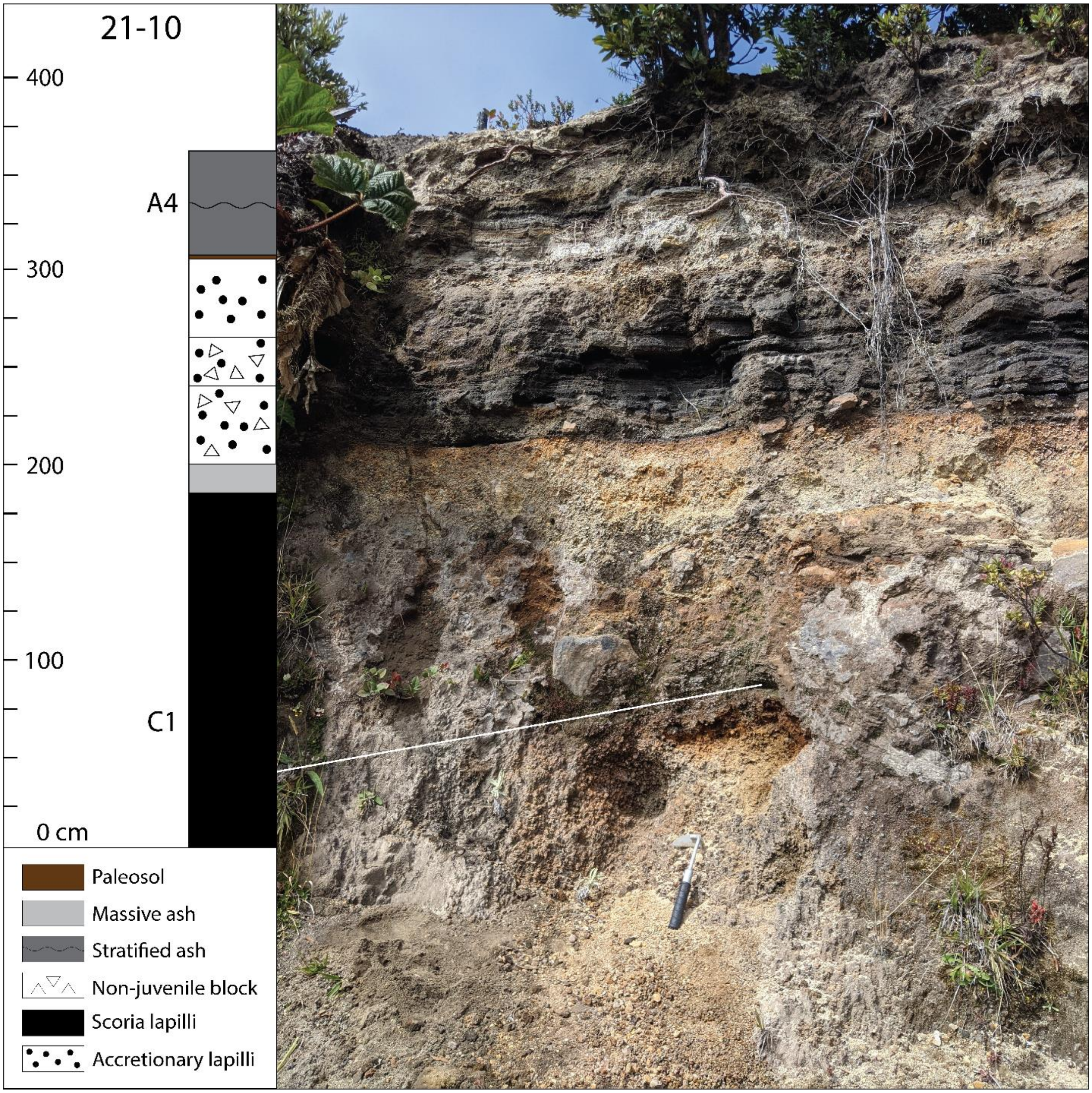

Figure 6 The key units of column 12-10 include C1 (relative age of ~1300 CE) and A4 (1963-1965 CE). The final placement of the remaining samples to the stratigraphy based on the chemical analysis is ongoing.

3.1.1 Column 21-04

The outcrop 21-04 illustrated in Figure 3 above, lies ~5.7 km S66W of the main crater and contains samples from the key units E1, E2, E4, and E5 (Figure 2). Campos-Duran and others (2024) dated three paleosols ranging in thickness between 5 and 20 cm. The paleosol sampled from the layer beneath E1 gave a carbon-14 date of 1620±30 yr. B.P. (~404 CE). The organic layer positioned between E4 and E5 was dated 1610±30 yr. B.P. (~414 CE). The third carbon-14 sampled from just above layer E5 was dated 1440±30 yr. B.P. (~584 CE). Although not sampled in this study, this outcrop comprises unit T. (U4), described by Clark and others (2006) as a subplinian ash and tephra lapilli deposit produced by the neighboring Turrialba Volcano around 25 CE. This tephra layer is significant as it is a marker horizon, helping to refine stratigraphy across outcrops. Based on the radiometric ages provided by previous research, the time elapsed between samples from unit E1 to E5 span nearly 90 years (~450 and ~540 CE).

3.1.2 Column 21-03

Located ~0.5 km SE of the Main Crater or ~50 m from the Irazú National Park entrance, column 21-03 is the largest outcrop at ~8 meters tall and ~5 meters wide. At the base of the outcrop is unit D1 (~700 CE). This stratified ash bed has been correlated to the below stratigraphy of column 21-06. As illustrated in Figure 4, carbon-14 sampling of the paleosol layer beneath D1 is dated 1300±30 yr. B.P. (age ~720 CE). Approximately 275 cm above unit D1 an additional organic layer dated at 1100±30 yr. B.P. (~1290 CE) by Campos-Duran and others (2024). Between unit D1 and the uppermost dated paleosol are units D2 (*~800 C.E*), D3 (*~850 C.E*), and D4 (~1000 CE). The uppermost layer, unit A4, is an ashfall deposit from the most recent, 1963-

1965 eruption, and is separated from unit A1 (an ash and scoria deposit from the 1723 eruption) by a ~5 cm paleosol layer.

3.1.3 Column 21-06

This area of stratigraphy is found ~5.7 km S43W of Irazú's main summit and contains the greatest number of qualified samples for geochemical analysis. This outcrop contains ~17 identifiable tephra layers, punctuated by layers of paleosols ranging in thickness from ~10 to ~100 cm. Unit D1 (~700 CE) is found ~1.5 meters from the base of the outcrop. Less than 2 meters above D1 is the most reoccurring layer, A4 (1963-1965 CE). Perhaps owing to the distance from the crater, is the ~60 cm thick layer of paleosol that caps the ~5.5-meter-tall outcrop (Figure 5).

3.1.4 Column 21-02

Situated 0.7 km S43W of the main crater is the sample area associated with section 21-02 (Campos-Duran et. al., 2024). Illustrated in Figure 6, the 130 cm base layer of this outcrop, Unit C1, has a relative age of ~1300 CE and has been correlated to column 12-10. Above this layer is unit C2 with a relative age of ~1420 CE Directly above C2 is a paleosol layer dated 510±30 yr. B.P. (calibrated age ~1510 CE). Similar to outcrop 12-03, the uppermost layer is a strombolian (VEI 3) deposit from the 1963-1965 eruption (A4).

3.1.5 Column 21-12

Column 12-12 outcrops ~3 km N24E of the main crater. The three carbon-14 dates have been sampled from this area by Campos-Duran and others (2024): 730±30 yr. B.P. (1290 ~ CE), 410±30 yr. B.P. (~1610 CE), and 0±30 yr. B.P. (1876-1916 CE). Notably, ~20 cm from the base of this outcrop is the subplinian Turrialba deposit. Based on these dated layers, the ages of the tephras sampled range from ~900 BCE and 1610 CE. A finalized stratigraphic column is currently in development.

3.1.6 Column 21-10

Approximately ~0.7 km S56W of the main crater is sample area 21-10 (Figure 7). While this outcrop has not been radiometrically dated, previous studies by Campos-Duran and others (2024) have identified the lowest layer as the strombolian lapilli and ash fall of unit C1 (~1300 CE) and the uppermost layer as the ash bed of unit A4 deposited in 1963-1965 CE

3.2 Geologic description of units

The six sample areas corresponding to the recent stratigraphy of Irazú include the following key layers or units: SSC (South Scoria Cones, D1 (700 CE), E1 (450 CE), E2 (460 CE), E4 (500 CE), E5 (540 CE), ECC (~1480-1640 CE), C1 (1300 CE), A1 (1723 CE), and A4 (1963-1965 CE). The following characterizes the physical and chemical properties, including the mineralogy of sampled tephras.

Table 3:Summary of sampled units and their stratigraphic position.

Stratigraphic ID	Unit	Age (CE)
1	SSC	77 - 232
5	E1	450
5.5	E2	460
6	E4	500
6.5	E5	540
11	D1	700
18	C2	1420
18.5	ECC	1480
24	A1	1723
26	A4	1963-1965

3.2.1 Southern scoria cones (SSC)

Directly ~5 km south of the Irazú main crater is a small cluster of four scoria cones ranging in age from 7097±30 yr. B.P. (6024-5912 BCE) to 18930±30 yr. B.P. (77-232 CE) based on the carbon-14 dates by Campos-Duran and others (2024). Parallel beds of alternating tephras and organic material ranging from ~ 3 cm to 1.5 m thick are commonly found throughout the SSC. This is most apparent within the oldest cone, the South Tower Cone, pictured in Figure 8. The 7 m tall and roughly 20 meters wide outcrop exposes continuous bed dipping 26°NW and a high degree of oxidation and hydrothermal weathering.

The bombs sampled from bottom to top illustrate the evolution of chemical weathering, with bombs collected from the lowest stratigraphic position exhibiting severe hydrothermal alteration in the form of tan-yellow-brown pockets (1-5 cm) that are soft and brittle to the touch. These samples also displayed swirling maroon bands (≤3 cm thick) within a bright red matrix of highly vesiculated glass. Although the red-to-black scoria samples all contained observable plagioclase (1-3 mm), tephras extracted from the uppermost layer of Perol contained noticeably more abundant grains of the mineral. Black lapilli samples taken from cones younger than Perol also displayed a high degree of hydrothermal alteration, likely exacerbated by the amount (~20%) of vesicles and coarser grains of plagioclase (~5 mm).

Figure 7: a) The South Tower cinder cone, 4.2 km S9W of the main crater. b) Pasquí is located 5.25km S2E of the summit. The 'x' marks the location of sampled lapilli.

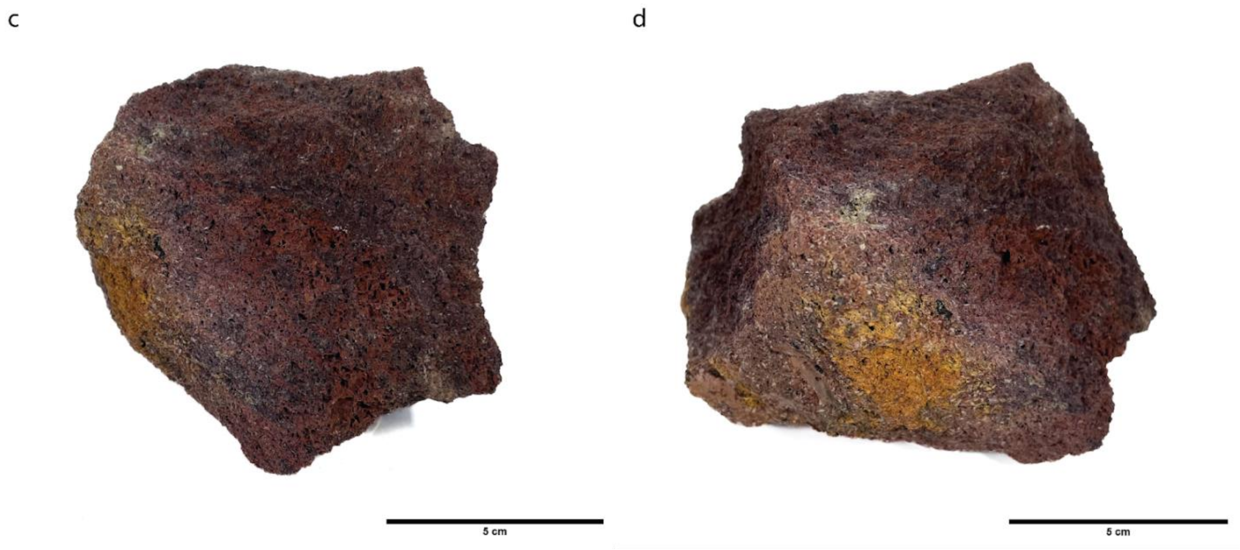

Figure 8: Tephra bomb sampled from the south tower cone exhibiting a swirling pattern (c) and hydrothermal alteration (d).

The mineralogy of these samples includes plagioclase (52.7-61.1%), orthoclase 10.7-12.6%, albite 27.7-31.6%)), pyroxene (18.6-20.7%), ilmenite (1.5-1.9%), and apatite (0.6-0.7%), which yields a TAS composition ranging from basaltic-trachyandesite to andesite. Further chemical analysis of the three qualified SSC tephras reveals an average composition of 55.49 wt.% SiO_2, 18.25 wt.% Al_2O_3, 7.53 wt.% Fe_2O_3, 7.43 wt.% CaO, 1.89 wt.% K_2O, 3.40 wt. % Na_2O, 4.74 wt. % MgO, 0.87 wt. % TiO_2, 0.12 wt. % MnO, and 0.27 wt. % P_2O_5, with a Ba range of 708-1045 ppm (Appendix A).

3.2.2 Units E1, E2, E4, & E5

The tephras sampled from units E1, E2, E4, and E5 are recorded in stratigraphic column 21-04 and express important historical eruptions at Irazú. In the field, these dark ash layers stand out against the silty organic-rich soils that separate them. As labeled in Figure 3, paleosols sampled by Campos-Duran and others (2024) temporarily constrain Units E1 through E4 between 1620± 30 yr. B.P. and 1440 ± 30 yr. B.P.

Located ~140 cm from the base of the outcrop is Unit E1. This ash bed is a 9 cm thick strombolian fallout composed of a medium-grained dark gray ash, deposited around 450 years ago (Clark et. al., 2006) and is topped by a 5 cm thick, poorly defined brown paleosol (Campos-Duran et. al., 2024). The succeeding unit, E2 (~460 CE), is a 10 cm thick layer of fine to medium-grained, gray ash that displays discontinuous wavy-like structures, up to 6 cm at its thickest point, of tan scoria lapilli. The pattern of interlayered paleosols continues, with a following ~15 cm bed of pale brown overlain by another ash bed (10 cm thick) and paleosol (15 cm thick). Above this is unit E4 (~500 CE), a ~10 cm thick bed of unevenly laminated gray to brown ash of medium to fine grain followed by a ~12 cm thick layer of soil. This paleosol shares an uneven erosional surface with the next layer, unit E5 (540 CE). E5 is a ~35 cm thick fine to medium-grained ash bed, penetrated by the roots of the overhead paleosols.

The units E1, E2, E4, and E5 are basaltic trachyandesite and basaltic andesite in composition, containing: 57.7-58.2% plagioclase, 10.7-12.6% orthoclase, 27.7-31.6% albite, 17.5-23.5% pyroxene, 1.8-2.1% ilmenite, and 0.7-0.9% apatite. Table X and Appendix X detail the XRF and ICP-MS results of all the layers sampled.

E1 is composed of 56.28 wt.% SiO_2, 18.10 wt.% Al_2O_3, 7.31 wt.% Fe_2O_3, 7.14 wt.% CaO, 2.07 wt.% K_2O, 3.55 wt. % Na_2O, 4.17 wt. % MgO, 0.96 wt. % TiO_2, 0.12 wt. % MnO, 0.29 wt. % P_2O_5; E2: 55.09 wt.% SiO_2, 17.94 wt.% Al_2O_3, 7.80 wt.% Fe_2O_3, 7.34 wt.% CaO, 2.12 wt.% K_2O, 3.71 wt. % Na_2O, 4.43 wt. %, 1.07 wt. % TiO_2, 0.14 wt. % MnO, and 0.37 wt. % P_2O_5; E4: 55.36 wt.% SiO_2, 18.53 wt.% Al_2O_3, 8.00 wt.% Fe_2O_3, 7.03 wt.% CaO, 1.95 wt.% K_2O, 3.29 wt. % Na_2O, 4.35 wt. % MgO, 1.04 wt. % TiO_2, 0.13 wt. % MnO, and 0.32 wt. % P_2O_5; and lastly, E5 (the average of two samples): 53.44 wt.% SiO_2, 18.21 wt.% Al_2O_3, 8.18 wt.% Fe_2O_3, 8.28 wt.% CaO, 1.86 wt.% K_2O, 3.37 wt. % Na_2O, 5.17 wt. % MgO, 1.04 wt. % TiO_2, 0.13 wt. % MnO, and 0.32 wt. % P_2O_5.

3.2.3 Unit D1

Unit D1 is a strombolian (VEI 2) fallout deposit from ~700 CE based on the underlying paleosol dated 1300±30 yr. B.P. (calibrated age ~720 CE) (Campos-Duran et. al., 2024) and an overlying layer (D2) that was correlated and dated 1230±30 yr. B.P (calibrated age ~800 CE). by Clark et. al., and others (2006).

In outcrop 21-04, unit D1 appears as a stratified bed of lapilli and coarse-grained ash, ~55 cm thick. Several tephra samples were collected from this outcrop for geochemical analysis below and above D1. These samples include a 40 cm thick stratified light gray to dark gray ash and dacitic lapilli extracted from beneath the first dated paleosol illustrated in Figures 3 and 4; a 40 cm parallel bed of stratified dark and light gray ash deposited >10 cm above D1; a 20 cm bed of dark gray, laminated ash ~60 cm above D1; a 50 cm even bed of loose, dark gray, coarse-grained ash (overlying ~150 cm D1), and finally the last sampled layer deposited ~280 cm above D1 is a stratified black and gray ash 30 cm thick.

Campos-Duran and others (2024) have correlated layer D1 to section 12-06 as well. Here, the unit outcrops display a lateral wedge of dark gray ash laminated with fine-grained lapilli, thinning into brown soil with a poorly defined erosional surface. Samples taken from below D1 include an 8 cm thick light to dark gray ash bed, ~15 to 20 cm brown ash eroding upward to soil; a 20-25 cm gray ash of fine to medium grain; ~30 cm bed of laminated gray and brown fine to medium grained ash, ~50 cm above D1 a massive ash bed (25-40 cm thick) was sampled as well, followed by a ~40 cm bed of ash appearing to transition into soil.

Unit D1 contains a TAS range of trachybasalt, basalt, and basaltic andesite with minerals including plagioclase (49.6-54.1%,) orthoclase (8.9-10.6%), albite (23.8-28.4%), pyroxene (16.2-30.8%), ilmenite (2.1-2.3%), apatite (0.8-0.9%), and olivine (0.0-16.4%). The mineralogy of all tephras samples from 12-04 and 12-06 are presented in Table X.

The average major element composition of unit D1 includes 51.06 wt.% SiO_2, 16.14 wt.% Al_2O_3, 8.97 wt.% Fe_2O_3, 9.01 wt.% CaO, 1.60 wt.% K_2O, 3.02 wt. % Na_2O, 8.55 wt. % MgO, 1.16 wt. % TiO_2, 0.14 wt. % MnO, and 0.35 wt. % P_2O_5.

3.2.4 Unit C2

Unit C2 observed in section 12-02 is a ~30 cm thick phreatomagmatic deposit consisting of massive ash primarily with hydrothermally altered lapilli of orange, brown, and gray poorly sorted throughout. The overlying, 4 cm thick paleosol sampled by Campos-Duran and others (2024) provides a carbon-14 date of 510 ± 30 yr. B.P. (calibrated age 1409–1434 CE). Below C2 is a 180 cm bed of coarse-grained black ash embedded with coarse scoria lapilli and bombs.

C2 contains plagioclase (55.1%), pyroxene (20.3%), orthoclase (7.1%), albite (24.9%), ilmenite (3.8%), and apatite (0.9%), with major and minor compositions of 53.43 wt.% SiO_2, 17.10 wt.% Al_2O_3, 9.70 wt.% Fe_2O_3, 7.69 wt.% CaO, 1.20 wt.% K_2O, 2.92 wt. % Na_2O, 5.40 wt. % MgO, 1.99 wt. % TiO_2, 0.15 wt. % MnO, and 0.40 wt. % P_2O_5. These XRF results are consistent with a basaltic andesite composition.

3.2.5 Unit A1

Irazú's largest recorded eruption (VEI ≤3) lasted from February 16, 1723, into December 1723 and is often described as a "violent strombolian" eruption, producing sustained ashfall and subsequent mudflows and deadly lahars (Alvarado, et. al., 2013). Alvarado and Schmincke (2013) have chronicled the eruption into three episodes: 1) phreatic, 2) strombolian, and 3) phreatomagmatic. Previous work by Campos-Duran and others (2024) has identified the resulting deposit as unit A1 and correlated the outcropping in sections 12-06 and 12-03.

Unit A1 is a 6-meter-thick coarse tephra deposit, primarily composed of laminated scoria lapilli, coarse ash, black to dark brown, and highly vesicular juvenile bombs that unconformably overtop a phreatic breccia deposit.

The mineralogy of basaltic andesite bombs, sampled by Alvarado (2013) contains 9.7-23.5% phenocrysts (based on 21 modal analyses expressed vesicle-free) with phenocrysts of plagioclase (55.1%), clinopyroxene (2.5-10%), orthopyroxene (0.7-2%), olivine (0.1-2.2%), opaques (0.1-1%), and groundmass (66.5- 90.3%). The geochemical results from the same report detail an average composition of 54.93 wt.% SiO_2, 17.09 wt.% Al_2O_3, 8.72 wt.% Fe_2O_3, 8.53 wt.% CaO, 2.21 wt.% K_2O, 3.17 wt. % Na_2O, 4.61 wt. % MgO, 1.17 wt. % TiO_2, 0.13 wt. % MnO, and 0.44 wt. % P_2O_5.

3.2.6 Unit A4

Unit A4 is an ash-rich PDC deposit corresponding to the VEI 3 eruption of 1963-65. This volcanic event emitted ash, blocks, and bombs, but no lava (Alvarado, 1993). The initial phase involved significant explosions, followed by alternating periods of explosive eruptions and steam emission (Murata et. al., 1966). Ash deposition occurred mainly westward from the summit toward San Jose, causing severe damage to agricultural lands and disrupting daily life in affected areas. The eruption peaked in December 1963 and January 1964, with voluminous ash and scoria ejected. Subsequent leveling surveys indicated significant upheaval of the volcano's upper part, followed by subsidence, suggesting a reduction in magma chamber pressure. Unit A4 is approximately ~ 55 cm thick of laminated light and dark gray medium to coarse-grained ash containing pulverized wall rock and fragments of scoria and pumice lapilli. Observed by Campos-Duran and others (2024) are rare very thin (<3 cm) fine ash phreatic deposits.

This historical tephra unit includes plagioclase (50.3-58.4%); orthoclase (9.6-14.8%), albite (26.2-31.9%), pyroxene (22.1-24.3%), ilmenite (1.8-4.1%), apatite (0.6-0.9%), and olivine (0-

6.2%). The erupted material consists of porphyritic two-pyroxene olivine basaltic andesite, with a consistent composition throughout the eruption (Alvarado & Schmincke 2013; Clark et. al., 1998, 2006; Murata et. al., 1966). Based on the XRF results of four samples from the 1963-1965 eruption, the major and minor elemental composition measured 53.25 wt.% SiO_2, 16.72 wt.% Al_2O_3, 8.47 wt.% Fe_2O_3, 8.85 wt.% CaO, 2.28 wt.% K_2O, 3.52 wt. % Na_2O, 5.31 wt. % MgO, 1.14 wt. % TiO_2, 0.14 wt. % MnO, and 0.31 wt.% P_2O_5.

3.2.7 Eastern cinder cone (ECC)

The eastern cinder cone group consists of three cones protruding 1.4-1.8 km east of the Main crater. Alvarado and Schmincke (2013) describe the most prominent cone, “Cono La Laguna,” as a deposit from the initial phreatic phase of the Strombolian eruption (VEI ≤2) that began on February 16, 1723. Commonly observed throughout the cones (Cono La Laguna, Tajo, and Torre) is a display of normal grading, with base layers embedded >10 cm, porphyritic bombs, waning into medium to coarse-grained lapilli, and topped with thick beds (~70 cm) of black and gray ash. The Cono La Laguna outcrop pictured in Figure 10 is notably bisected by a 5-15 cm thick layer of tan to light gray consolidated lapilli (>3 cm), highlighting a highly vesiculated (>20%) scoria bomb extracted from the bed of the lowest stratigraphic position that contains fine to coarse grains of plagioclase suspended in a black to dark gray glassy matrix. The lapilli tephras observed throughout the ECC range from 1 mm to 15 mm in diameter. The amount and size of the gaseous cavities vary with the largest vesicles measuring >5 mm.

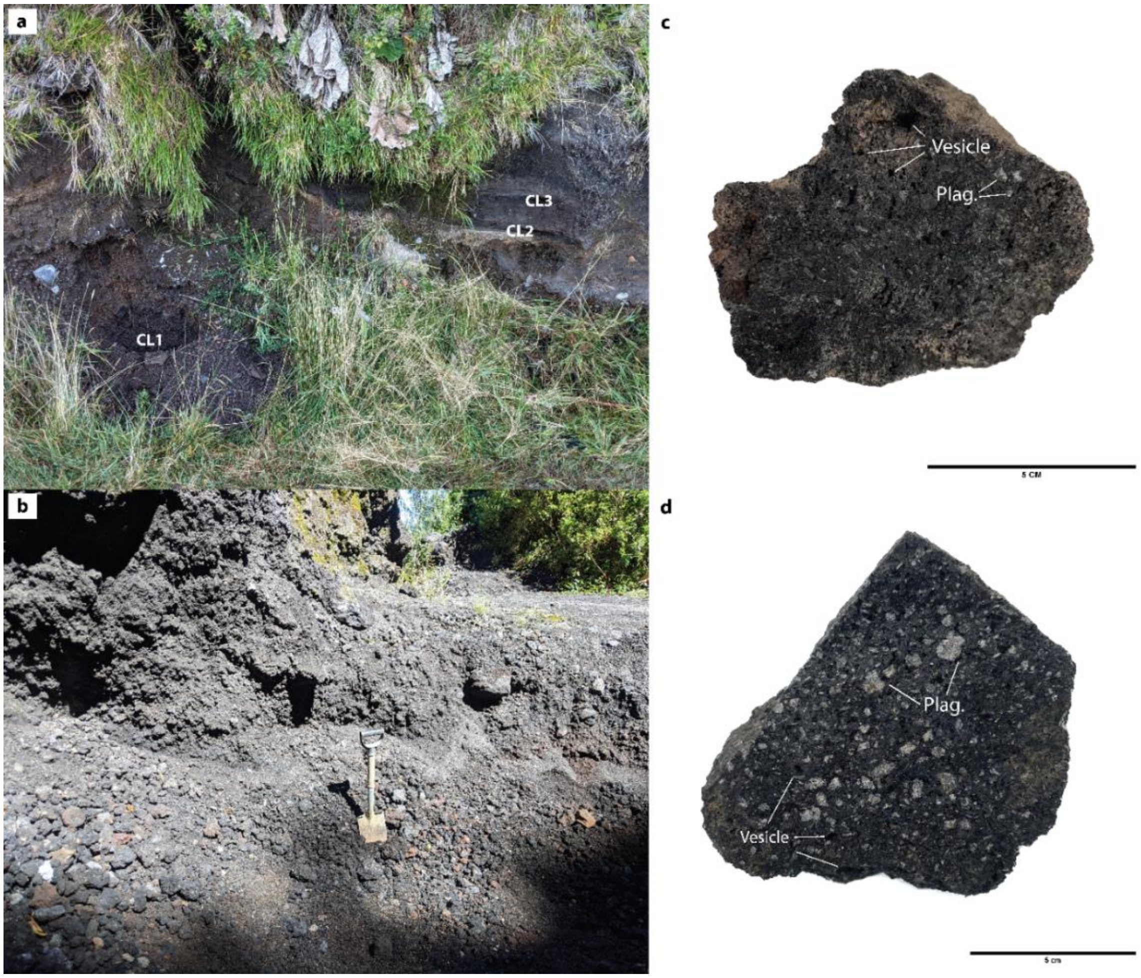

Figure 9: (a) Outcrop photo of Cono La Laguna where samples CL1, CL2, and CL3 were collected for geochemical analysis. (b) Tajo scoria cone outcrop. (c) ~10 cm scoria bomb with fine to coarse grains of euhedral to subhedral plagioclase. (d) Porphyritic block from the Tajo scoria cone with very coarse grains of plagioclase.

A total of five tephra samples provided conclusive chemical results. The following major and minor element compositions are the averages of the five tephras: 54.24 wt.% SiO_2, 17.79 wt.% Al_2O_3, 8.14 wt.% Fe_2O_3, 8.03 wt.% CaO, 1.87 wt.% K_2O, 3.43 wt. % Na_2O, 5.10 wt. % MgO, 1.00 wt. % TiO_2, 0.13 wt. % MnO, and 0.27 wt. % P_2O_5. The CIPW normative mineralogy calculation measures: plagioclase (53.8-59.6%), pyroxene (19.4-24.5%), orthoclase (10.0-12.8%), albite (24.8-33.5%), ilmenite (1.8-2.0%), apatite (0.5-0.7%), and less than 2% olivine.

3.3 XRF results

The XRF results from tephras sampled in 2021 have been analyzed in combination with the results produced by Alvarado (1993) and Clark et. al., (1998). This larger scope of samples makes for a most robust chemical analysis. The average concentrations of major and minor elements of the key units previously identified are listed in Table 4, including the 1723 CE samples analyzed by Alvarado (1993).

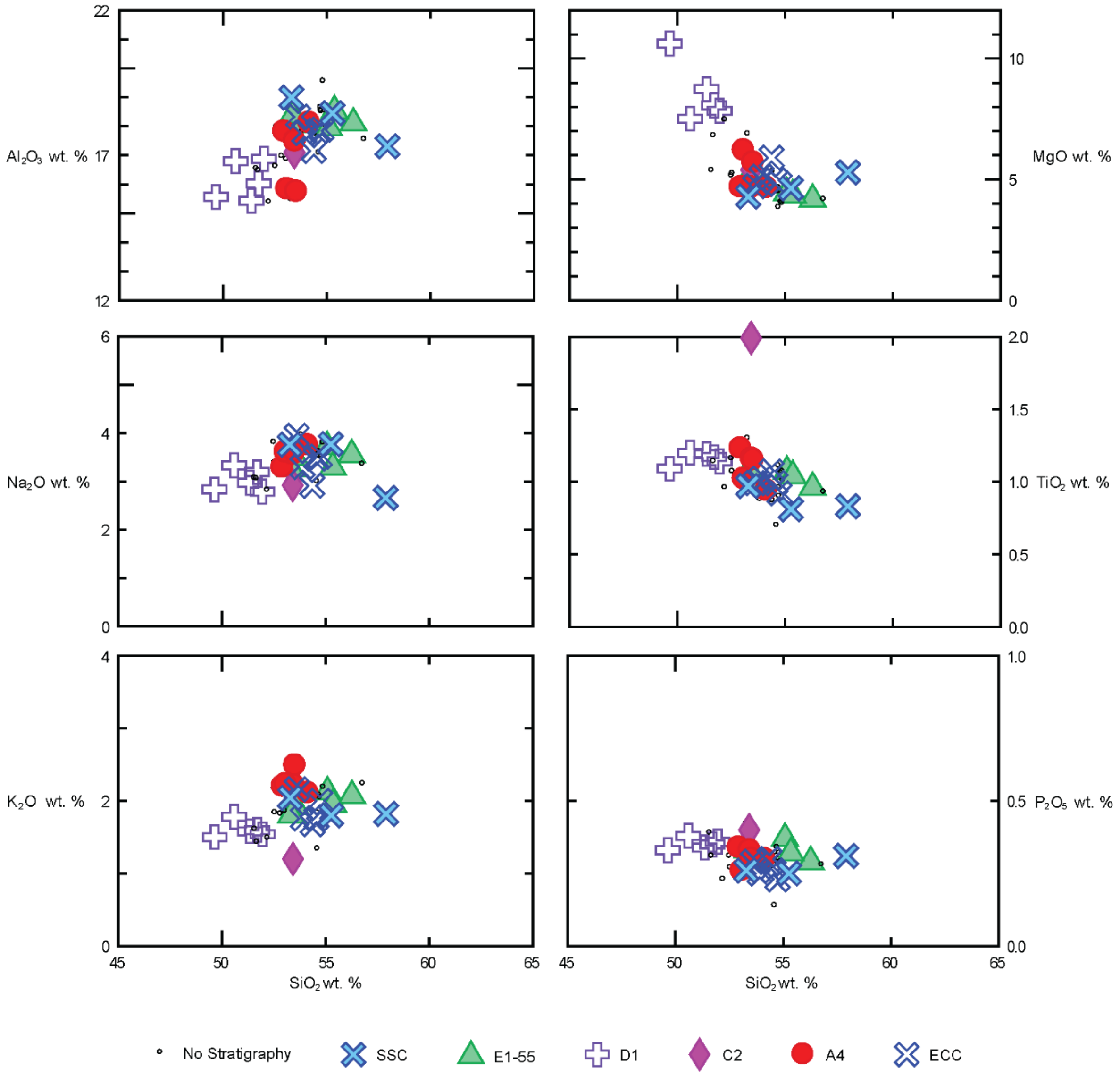

Figure 10: Harker variation diagrams for the samples corresponding to identified units.

The Harker diagrams in Figure 10 illustrate a noticeable influx of MgO in the samples pertaining to unit D1 (~700 CE), with weight percentages ranging from 7.51 to 10.62. This enrichment stands out against the average MgO wt. % of 5.31 was observed across the bulk of samples. In the period prior to the deposition of unit D1, MgO concentrations were nearly half this (3.85 to 5.33 wt. %). The average concentration of K2O is 2.04 wt. %. As seen in Figure 11 below, most tephra samples present K2O and SiO2 values consistent with the high-potassium calk-alkaline magma series. The main exceptions to this are unit C2 with a K2O wt. % of 2.92 and a single SSC sample with a K2O wt. % of 2.04.

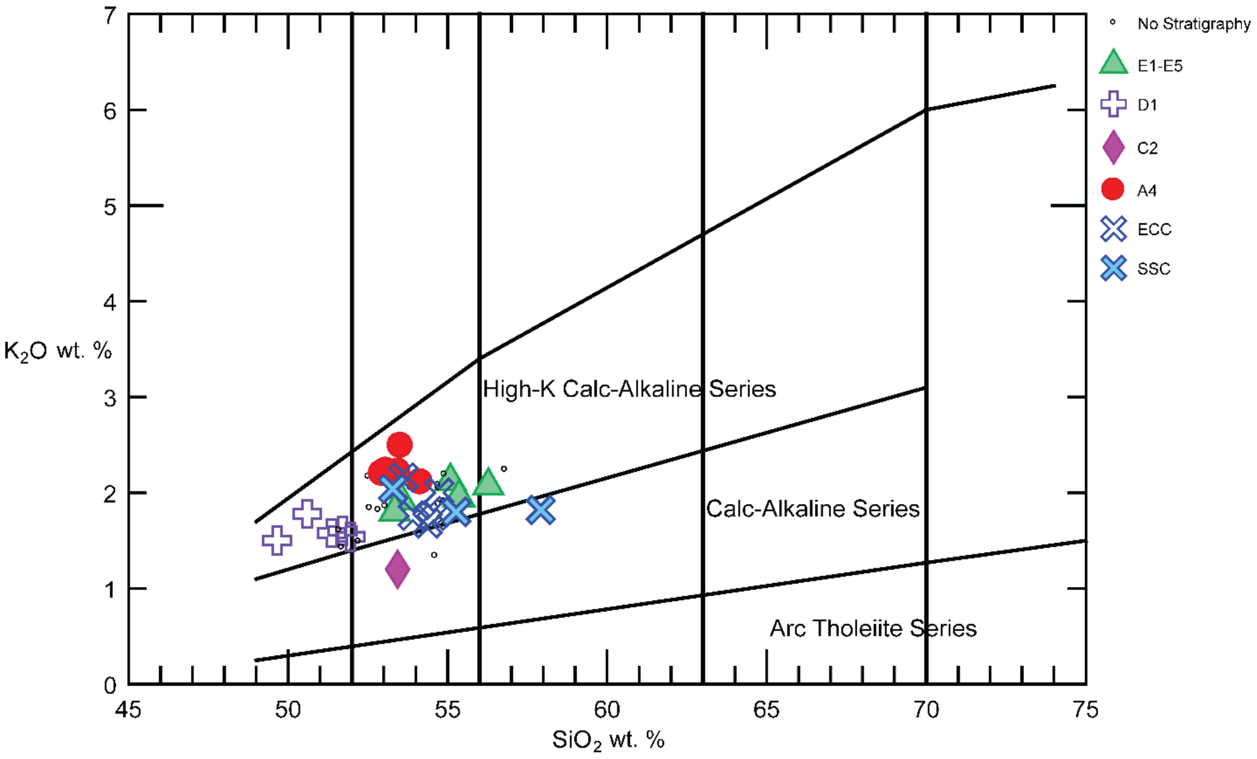

Figure 11: SiO_2 vs. K_2O diagram.

Additionally, total alkali (Na_2O+K_2O) concentrations fluctuate between ~1.5 and ~6 wt. %, with the highest concentration occurring around 800 and 1500 CE. These values contrast with the average 4.5 wt. %. Figure 12 shows the total alkali-silica (TAS) scatterplot, indicating basaltic trachy-andesite and basaltic andesite rock types.

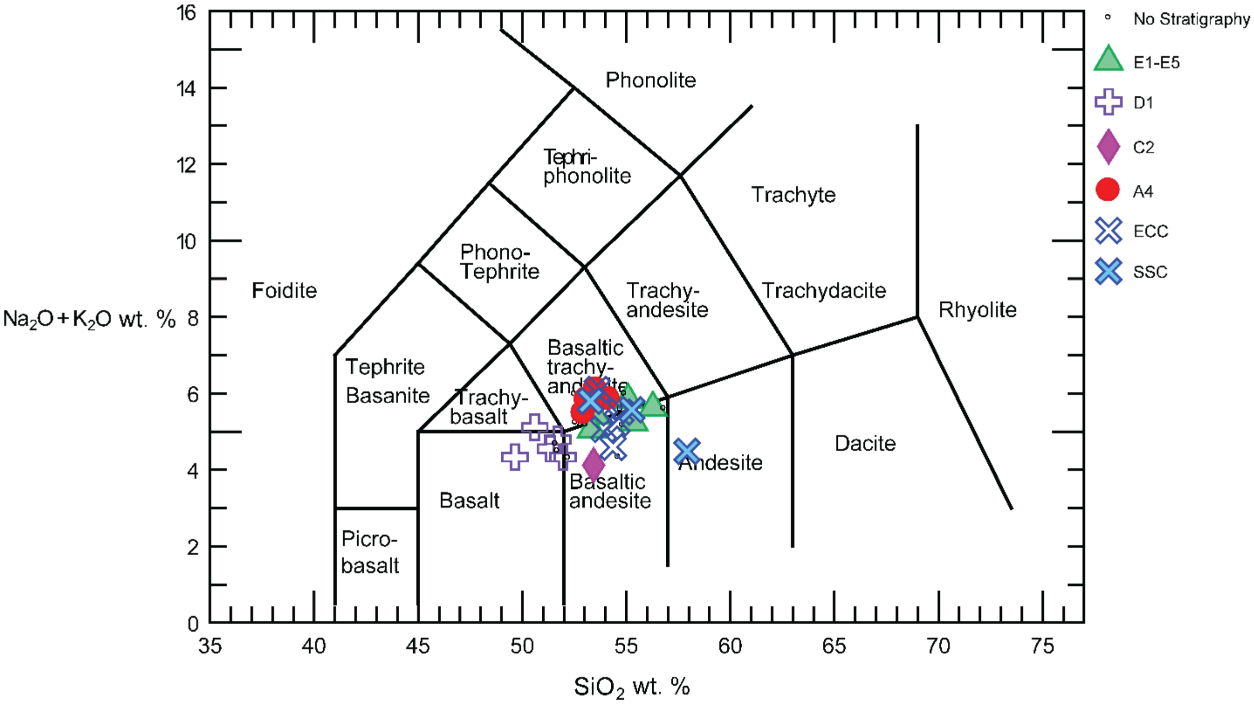

Figure 12: TAS diagram of Irazú tephras over the last ~2,400 years.

Based on the major and minor compositions, the normative mineral assemblage can be plotted within the basalt tetrahedron (Figure 13) to chemically characterize the types of basalt sampled at the Irazú Volcano. The subalkaline basalts plot to the right of the plane of silica saturation where silica polymorphs are stable.

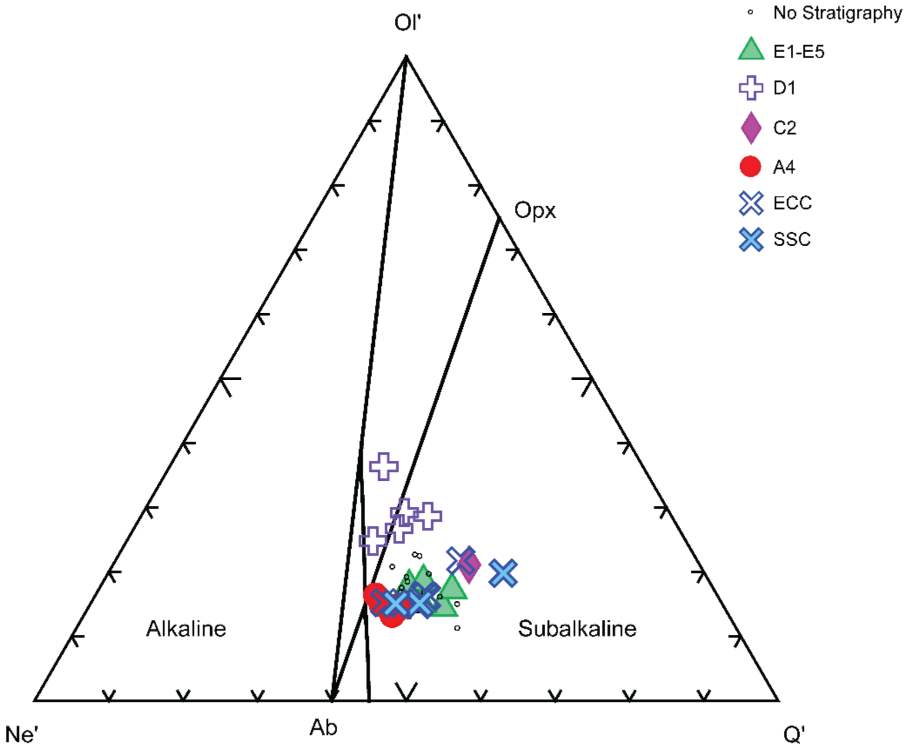

Figure 13: Base view of the basalt tetrahedron. Ol'-olivine; Opx- orthopyroxene; Q'-quartz; Ab-albite; Ne'- Nepheline.

The tephra samples were also analyzed using an AFM diagram (Figure 14), a ternary diagram displaying the relative proportions of the oxides Na2O + K2O (A), FeO + Fe2O3 (F), and MgO (M). Based on this, we see the Irazú samples are aligned with calc-alkaline magmas, which are typically more oxidized compared to tholeiitic magmas. This higher oxidation state promotes the early crystallization of iron oxides such as magnetite. As a result, the iron content of the magma can remain relatively steady during cooling because a portion of the iron is sequestered into the magnetite rather than being incorporated into other minerals or remaining in the melt. This behavior contrasts with tholeiitic magmas, where iron tends to remain in the melt until later stages of cooling, leading to a more pronounced decrease in iron content over time (Winter, 2001).

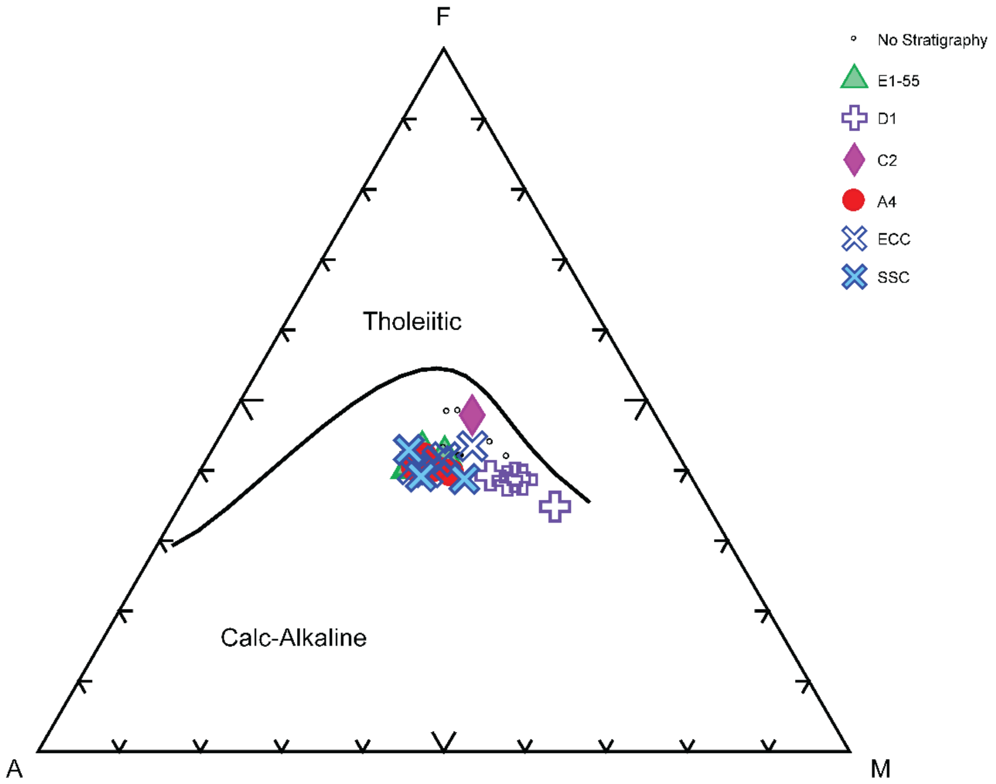

Figure 14: AFM diagram of tephras sampled from Irazú Volcano displaying a calc-alkaline arc magma series.

3.4 ICP-MS results

Trace and rare earth element concentrations measured by ICP-MS were analyzed with an emphasis on the large ion lithophile elements (LILE) and high-field strength elements (HFSE). Key trends within these trace element subgroups can implicate magmatic processes such as subduction influence, partial melting, and crustal accretion.

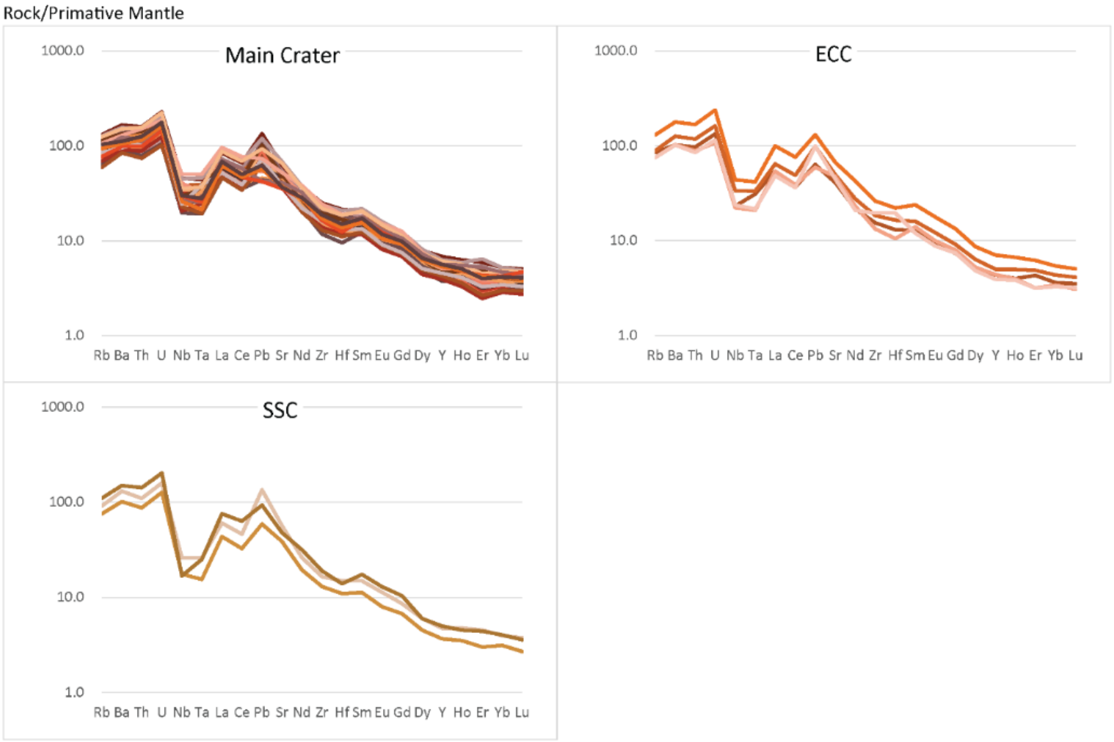

Figure 15: Spider diagram showing a depletion of the progressively incompatible REEs, normalized to primitive mantle concentrations.

As far as the LILE are concerned, the concentration of Rubidium (Rb) varies from 59.18 to 130.84 ppm across samples, Barium (Ba) also shows variability, with concentrations ranging from 84.21 to 177.56 ppm. Thorium (Th) and Uranium (U) show relatively high concentrations, with Th ranging from 74.03 to 167.42 ppm and U ranging from 134.40 to 194.56 ppm. This enrichment is observed in the trace element spider diagram, Figure 15.

The concentrations of zirconium (HFSE) are notably high in some samples (e.g., 123.07 ppm) with a range of 131.32 to 307.70 ppm. Niobium (Nb) ranges from 16.81 to 50.01, with an average of 19.56 ppm and Tantalum (Ta) ranges from 0.63 to 2.86, averaging 1.28 ppm. Hafnium (Hf) ranges from 2.95 to 6.61 ppm, with an average of 4.73 ppm.

Figure 16 displays a normalized REE diagram with similar concentrations of lanthanide series elements across the main crater, SSC, and ECC samples over time. The trace and REE data reveal significant variations in element concentrations, pointing to complex magmatic processes involving subduction influence, partial melting, and crustal contamination.

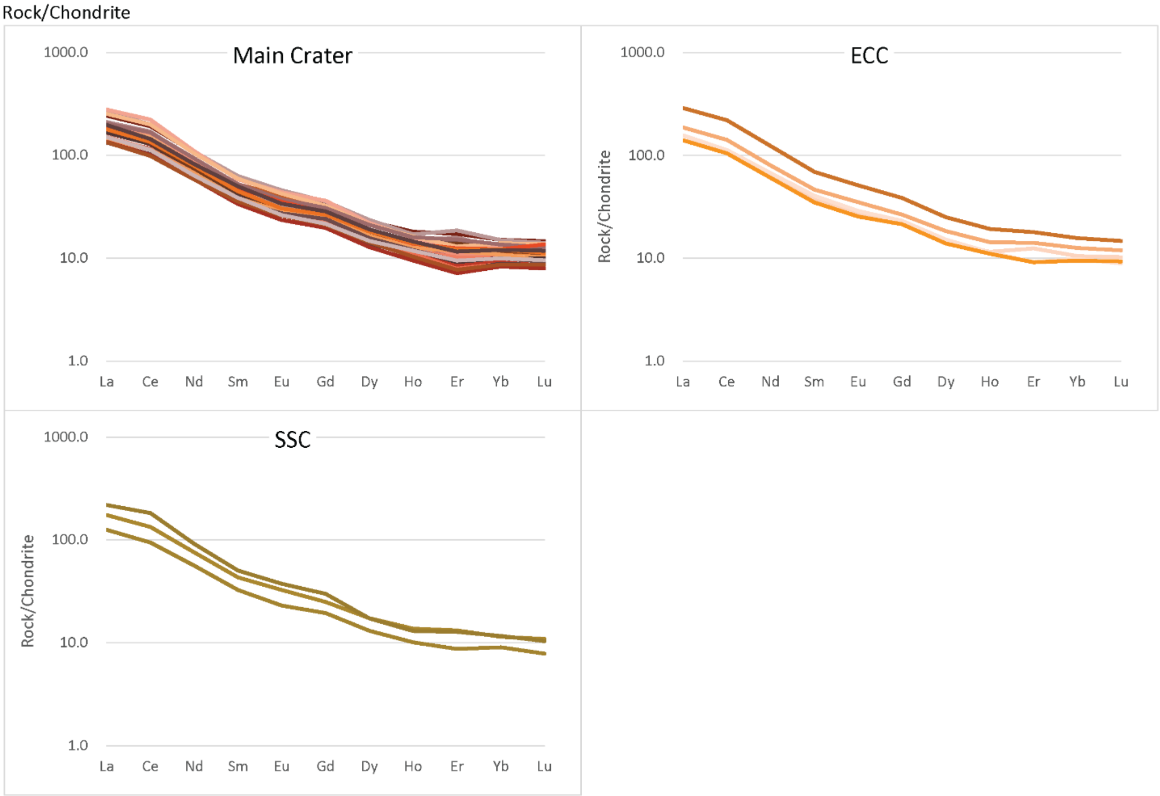

Figure 16: Chondrite-normalized REE diagram of the main crater, ECC, and SCC samples. Normalizing factor from McDonough and Sun (1995).

Table 4: Major, minor, and trace element composition of key stratigraphic layers.
A complete list of key units is provided in appendix A.

Unit	SSC	E1	E2	E4	E5	DI	C2	ECC	A1	A4
Sample ID	*avg. of 3 samples	CV2	CV3A	CV3B	*avg. of 2 samples	*avg. of 5 samples	*avg. of 2 samples	*avg. of 5 samples	*avg. of 15 samples	*avg. of 4 samples
Age (CE.)	77 - 232	450	460	500	540	700	1420	1460-1680	1723	1963-65
Sample type	Lapilli	Ash	Ash, lapilli	Ash	Laminated ash	Ash, lapilli	Ash, lapilli	Lapilli	Scoria	Ash
Wt. %										
SiO2	55.49	56.28	55.09	55.36	53.44	51.06	53.43	54.24	53.93	53.25
TiO2	0.87	0.96	1.07	1.04	1.04	1.16	1.99	1.00	1.17	1.14
Al2O3	18.25	18.10	17.94	18.53	18.21	16.14	17.1	17.79	17.09	16.72
Fe2O3	7.53	7.31	7.80	8.00	8.18	8.97	9.7	8.14	8.72	8.47
MgO	4.74	4.17	4.43	4.35	5.17	8.55	5.4	5.10	4.61	5.31
CaO	7.43	7.14	7.34	7.03	8.28	9.01	7.69	8.03	8.53	8.85
Na2O	3.40	3.55	3.71	3.29	3.37	3.02	2.92	3.43	3.17	3.52
K2O	1.89	2.07	2.12	1.95	1.86	1.60	1.2	1.87	2.21	2.28
MnO	0.12	0.12	0.14	0.13	0.13	0.14	0.15	0.13	0.13	0.14
P2O5	0.27	0.29	0.37	0.32	0.32	0.35	0.4	0.27	0.44	0.31
Trace (ppm)										
Sc	20.61	21.69	17.34	17.06	20.58	23.90	22.38	26.18	15.69	22.01
V	229.30	234.46	178.30	174.57	238.21	200.19	298.01	252.76	221.87	198.97

Cr	106.37	67.10	70.46	91.28	121.17	284.59	225.87	112.91	76.33	95.68
Mn	942.00	1128.91	912.84	883.76	995.35	1088.99	1070.23	1157.10		981.75
Co	24.43	27.77	25.61	25.60	26.35	35.79	37.94	30.95	21.50	24.39
Cu	101.42	102.70	56.72	119.38	98.85	71.56	268.06	112.34	115.13	97.92
Zn	78.86	96.87	53.37	79.76	76.89	65.36	87.52	93.09	130.11	81.30
Ga	21.58	23.59	18.32	19.18	20.03	20.35	25.14	23.93	18.33	19.63
As	4.20	4.47	3.99	3.56	3.15	3.34	5.47	4.17	13.00	3.22
Rb	58.60	68.12	53.74	47.75	49.42	44.34	42.31	57.61	51.93	58.28
Sr	1004.28	1101.61	846.65	946.24	991.82	939.90	1094.71	1049.10	821.33	795.09
Y	20.31	23.22	20.55	19.66	19.78	21.42	39.02	22.46	24.56	24.95
Zr	180.33	206.08	191.92	185.68	166.11	175.26	307.70	208.02	213.93	197.50
Nb	14.39	21.16	22.28	20.85	19.79	26.05	32.87	20.86	17.89	19.90
Mo	2.48	2.90	2.41	2.57	1.55	1.94	2.68	2.38	3.20	1.88
Sn	2.32	1.09	1.07	0.65	0.51	0.93	6.08	1.07		0.88
Cs	0.57	0.83	0.64	0.42	0.47	0.50	0.42	0.61		0.71
Ba	888.64	907.70	730.66	717.63	743.18	697.70	889.57	853.19	841.73	766.17
La	41.09	45.43	42.72	39.62	40.85	44.47	73.45	44.05	33.67	45.40
Ce	83.91	91.06	83.69	82.16	81.55	90.34	170.63	83.88	61.22	89.17
Nd	34.84	36.69	33.45	34.50	34.17	38.78	73.72	36.68	26.44	39.26
Sm	6.44	7.00	6.23	7.09	6.37	7.31	13.99	6.97	8.83	7.48

Eu	1.80	1.96	1.64	1.84	1.80	2.04	4.07	1.95	<8	1.99
Gd	5.10	5.25	4.75	5.24	4.97	5.78	11.69	5.39		5.84
Dy	4.04	4.27	3.80	4.11	3.95	4.38	8.21	4.42		4.86
Ho	0.70	0.74	0.68	0.71	0.68	0.73	1.36	0.77		0.83
Er	1.91	1.76	2.06	2.15	1.78	1.86	3.63	2.08		2.13
Yb	1.82	2.07	1.63	1.88	1.72	1.76	3.05	1.98		2.13
Lu	0.25	0.28	0.24	0.27	0.24	0.24	0.38	0.28		0.32
Hf	4.10	4.64	4.43	4.50	4.04	4.08	5.78	5.05		4.30
Ta	0.91	1.18	1.26	1.15	1.11	1.37	2.86	1.21		1.03
Pb	6.78	5.52	6.21	7.23	4.96	4.29	5.40	6.40	7.25	3.61
Th	9.61	11.01	9.73	9.91	9.22	7.76	8.45	9.44	12.33	9.55
U	3.41	3.87	3.26	3.51	3.06	2.59	3.07	3.17	<3	3.33

4 DISCUSSION

The elemental composition of the Irazú tephra samples indicates a primitive, continental magma source, with samples ranging from basalt to andesite, including intermediate types such as basaltic trachyandesite and basaltic andesite. A closer examination of trace and rare earth element (REE) concentrations suggests a complex magmatic evolution. By integrating geochemical data with the stratigraphy of Irazú, a chronological analysis of the tephra samples becomes possible. This discussion explores the chemical variations in major, minor, and trace elements to elucidate the potential magmatic processes at play in the Irazú volcanic system. Additionally, it provides a comparison with previous studies, discusses the limitations of current research, and suggests directions for future investigations.

4.1 Chemical Variation

To achieve a more complete geochemical analysis, major and trace element values were incorporated from previous work. This includes major and some trace element data for both the 1723 and 1963 eruptions from Alvarado (1993) and major and trace element data from Clark et. al., (1998). These tephra samples are included in the plots where applicable.

4.1.1 Major and minor elements

The major and minor wt. % oxides are organized based on their stratigraphic positions (Figure 17) and analyzed for temporal trends. With a wt. % range of 10.47%, MgO has the most prominent temporal variations. Most notable are the two periods of enrichment around 700 and ~1000 CE. Each peak is preceded by a period of MgO depletion accompanied by an increase in CaO. The fluctuation of calcium oxides displays three consecutive trends with a 2-3 wt. %

increase in CaO followed by a depletion of 3 wt. % on average. These inferred cycles are punctuated by two points of depletion at 6.71 wt. % (deposited before unit D1) and 5.40 wt. % of unit C2 (~1420 CE). Typically, this enrichment of MgO and CaO would indicate a less evolved mantle source.

However, given Irazú's magma chamber depth of an estimated 1,500 m to 1.8 km (Murata et. al., 1966; Alvarado, 1993; Hudnut, 1983) it is unlikely that the enrichments of CaO and MgO represent the crystallization of olivine, clinopyroxene, and plagioclase but rather the accumulation of these minerals sourced from the crystal-liquid network, encasing the shallow magma chamber. This cumulate lining emplaced by earlier eruptions, was likely disturbed during volcanic activity, flushing these more mafic minerals into the newer melt influx and raising the compositions of CaO, MgO, and other elements with an affinity to those minerals (Kruger and Latypov, 2022).

Unit C2 (~1420 CE) and an unnamed unit given an approximate age of 1300CE by Campos-Duran and others (2024) display relatively high concentrations of TiO_2 at ~2%. These brief periods of enrichment coincide with the accumulation of titanium-bearing minerals such as ilmenite found in the liquid-crystalline mush encasing the magma.

Total alkali (Na2O+K2O) concentrations oscillate with 5 notable peaks of around 6 wt. %. These brief periods of enrichment are punctuated by depleted values (~4 wt. %). The elevated Pearce element ratios plotted in Figures 18c, d, and suggest the accumulation of plagioclase along the chamber walls.

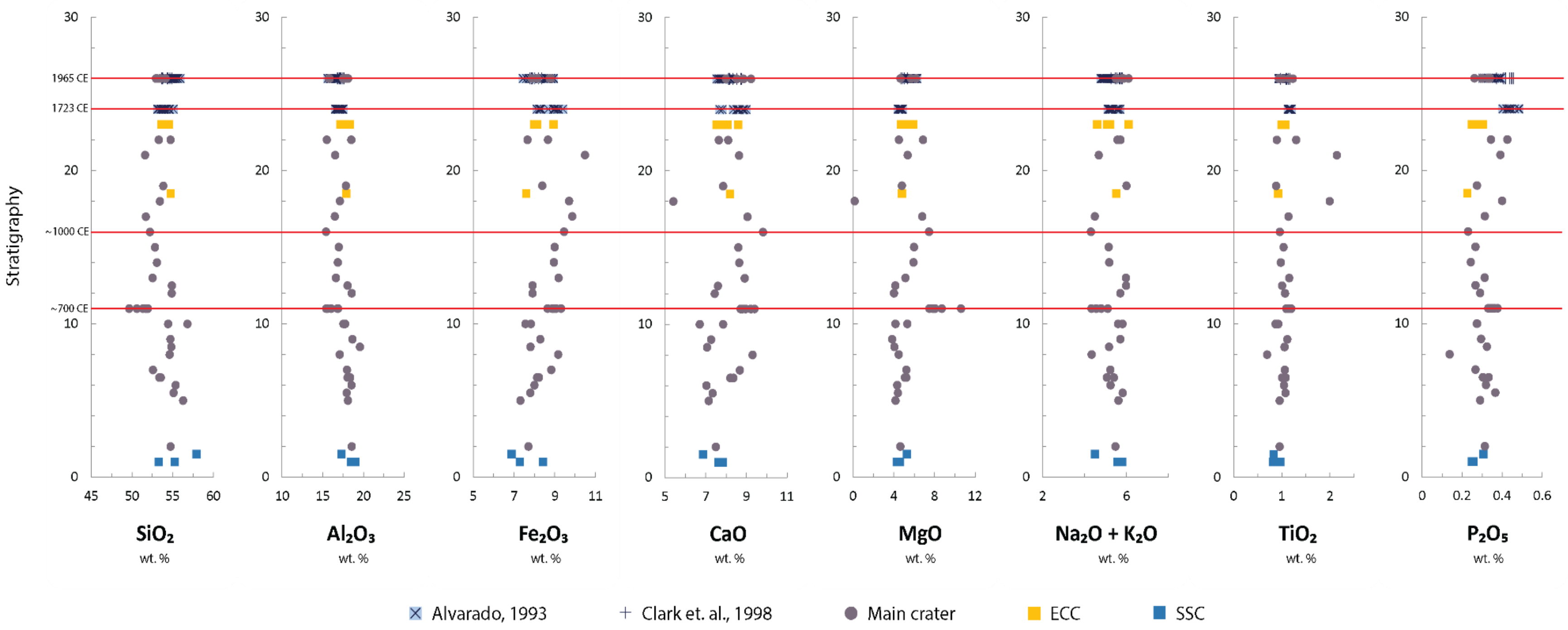

Figure 17: Major and minor wt. % oxides of tephras plotted against their stratigraphic position. Important historical eruptions, occurring around 700 CE, 1000 CE, 1723 CE, and 1963 CE, are indicated by the horizontal red lines.

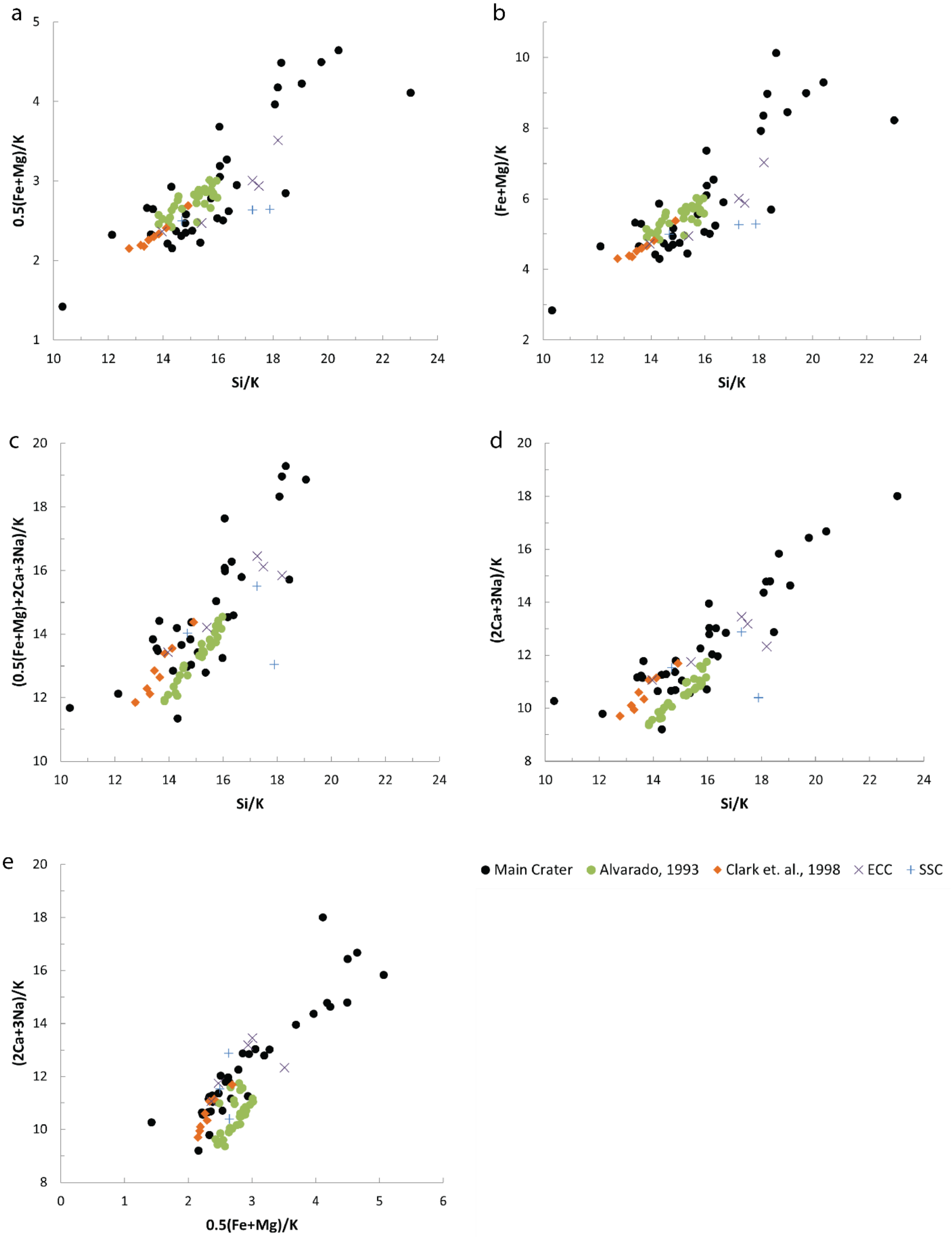

Figure 18: Pearce element ratio diagrams of the basaltic andesite tephras of Irazú.

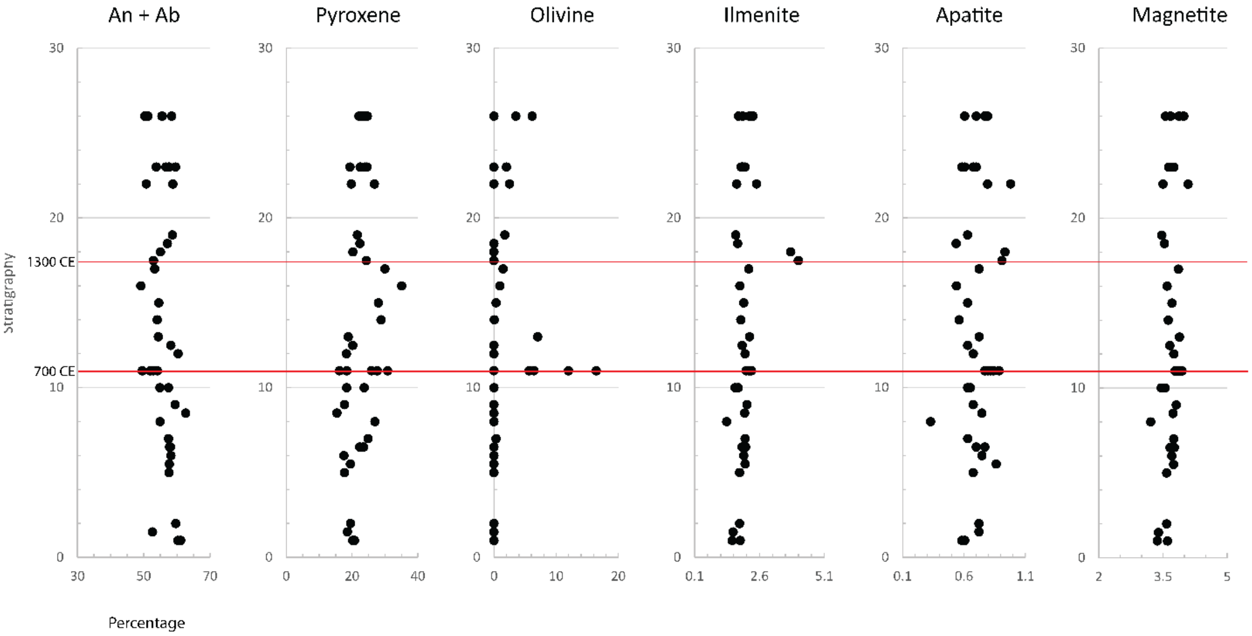

Figure 19: CIPW normative mineral compositions versus its stratigraphic position. Key dates highlighted.

The cinder cone groups ECC and SSC share similar major and minor element compositions despite occurring nearly 1500 years apart. This could indicate that both clusters share the same magma chamber or a chemical marker signifying the beginning and end cycle of Irazú's magmatic recharge.

The CIPW normative mineral diagrams are shown in Figure 19. Here, samples on average contain 56% plagioclase, 23% pyroxene, 4% magnetite, 2% ilmenite, and 0.7% apatite. Olivine is minimal throughout most of Irazú's recent eruptive history, apart from unit D1. Two tephras approximately dated 1300 and 1420 CE exhibit high ilmenite minerals. The variability of plagioclase and pyroxene, with sporadic interjections of olivine, support the notion that this seemingly primitive melt is actually the perturbation of the pre-existing crystals that separate the interior convecting liquid, and the outer solid cumulates (Kruger and Latypov, 2022).

4.1.2 Trace and REE ratios

Trace and REE ratios are sensitive to chemical fractionation due to their partitioning coefficients, fractionation patterns, the melting process, and the interaction between the melt and crust. The ratios listed in Table 5 offer insight into Irazú’s geochemical history including its source characteristics, the degree and type of partial melting, and subsequent fractional crystallization and contamination processes (Goss et. al., 2006).

Table 5: Trace element ratios
These ratios include samples from this work and Clark et. al., 1998.

La/Sm	4.78-7.4
La/Nb	1.18-4.33
La/Yb	18.57-29.25
Zr/Nb	5.88-29.21
Y/Nb	0.71-1.9
Ba/Nb	14.92-87.2
Ba/Rb	11.85-21.02
Ba/Th	70.06-105.31
Ba/La	12.11-23.71
Sr/Zr	2.85-6.72
Rb/Sr	0.04-0.09

Lanthanum to Samarium (La/Sm) ratios range from 4.78-7.4 which suggests enrichment in light REEs (LREEs), likely indicating a source enriched in LREEs. Lanthanum/Niobium (La/Nb) ratios (1.18-4.33. A higher La/Nb ratio reflects a subduction-related source, while lower ratios are more typical of mid-ocean ridge basalts (MORBs). Zr/Nb (5.88-29.21) and Y/Nb (0.71-1.9) ratios characterize a magma source consistent with fluid-controlled alkaline basalts (Rollinson, 1993; Pearce & Peate, 1995).

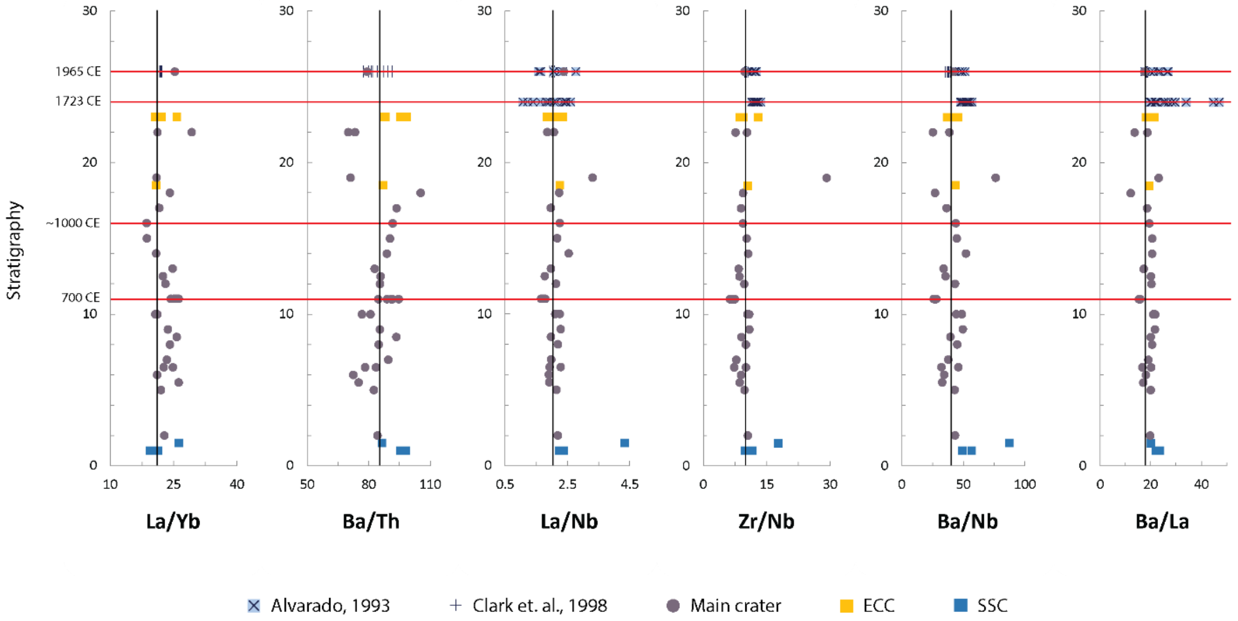

Figure 20: Trace element ratios versus their stratigraphic position, with key dates (horizontal red lines) associated with units D1 (700 CE.), A1 (1723 CE.), and A4 (1963 CE.). Vertical lines indicate the REE ratio averages.

High ratios of Ba/Nb are indicative of a subduction zone environment, where fluid from the subducting slab introduces Ba into the mantle wedge, while lower ratios are more common in OIBs and MORBs (Alvarado, 1993; Clark et. al., 1998; Herbert et. al., 2009). The Irazú samples collected cover a broad range of Ba/Nb ratios (14.92-87.2), echoing its complex tectonic history. Since Barium (Ba) is more mobile in fluids compared to Rubidium (Rb) Thorium (Th), and Lanthanum (La), these ratios provide insight into the influence of fluids on Irazú's magmatic evolution. The moderate Ba/Rb range of 11.85 to 21.02, Ba/Th (70.06-105.31), and Ba/La (12.11-23.71) suggest less extensive fractionation consistent with alkaline basalts and the presence of subduction slab fluid (Rollinson, 1993; Tatsumi & Eggins, 1995; Thompson & Morrison, 1998).

4.1.3 Implication for magmatic processes

The varying concentrations of LILEs and HFSEs imply a complex magmatic process, congruent with Costa Rica's tectonic activity. Elevated trace element ratios (Ba/Th, Ba/Nb, and La/Yb) are indicative of subduction-related fluids breaching and interacting with magma. Meanwhile, the presence of high HREE suggests a mixed or evolved source of magma, possibly involving both lithospheric mantle and asthenosphere components (Rollinson, 1993; Tatsumi & Eggins, 1995; Thompson & Morrison, 1998, Winter, 2001).

Ash, lapilli, and bombs sampled from Irazú spanning the last ~2400 years, appear to display low to high degrees of influence by the subducting slab fluids percolating the Central Costa Rican Deformation Belt. Samples dated ~0 CE. and ~1400 relatively, show moderate influence, while samples from the 1723 eruption contain an enrichment of Ba likely a result of subducted sediments. These periods contrast the interpretation of unit D1 (~700 CE.). Based on La/Sm ratios in Appendix A.1 and the relatively shallow depth of the magma chamber, rather than being the result of the partial melting of mantle material, it is more likely that an observable spike in mafic material is indicating a flush of primitive melt

4.2 Comparison of previous studies

This study marries a high-resolution geochemical technique with tephrostratigraphy to characterize Irazú's eruptive history over the last ~2400 years. Previous studies lack high-resolution geochemical analysis of the tens of VEI ≤2 eruptions leading up to the 1723 Strombolian eruption. Modeling chemical data from the 1723 and 1963-65 eruptions is important to understand Irazú's current behavior, however, to prepare robust and accurate eruptive projections, a broader sampling of historical eruptions is required.

This work advances the understanding of volcanic activity and geochemical evolution by sampling tephras from ~0 CE to present for major and trace element variations and mineral fractionation and comparing suitable samples to known eruptions.

4.3 Limitations and future research

This study acknowledges several limitations that may impact the interpretation of its findings. Firstly, the lack of grain size analysis restricts our understanding of tephra-dispersion and eruptive dynamics (Pioli et. al., 2005). Despite the breadth of samples collected in the field, the stratigraphic correlation is limited in outcrops where exposure is high and leads to extensive weathering of potential samples, which makes it very difficult to draw comprehensive conclusions about temporal changes. While ICP-MS provides valuable data, its lower spatial resolution compared to EMPA limits detailed chemical analysis of the mineral suite. Moreover, Ni, Ge, Se, Cd, Sb, Te, Pr, Pm, Tb, W, and Tl were excluded from the chemical results due to their absence in USGS standards or the need for more robust detection methods, which may lead to an incomplete geochemical profile. These limitations must be considered when interpreting the study's outcomes.

Factors that may affect the interpretation of results include the chemical weathering and hydrothermal alteration of tephras. Large ion lithophiles, such as Ba and Sr, are susceptible to chemical weathering, as these salts are more mobile and are prone to leaching from their crystal lattice with extensive exposure to water. This can significantly alter the original composition of sampled tephras, complicating geochemical analysis. Additionally, sampling beyond recent volcanic activity presents challenges due to the partial or total erosion of deposits or their burial under more recent layers, which obscures older tephras. Dense vegetation can also limit outcrops and poorly preserved tephra layers, making it difficult to obtain representative samples.

Future research could enhance the current findings by establishing a collaborative relationship with the residents of Irazú Volcano. Sharing these findings with the local community and learning from those who have lived with the volcano for generations would help bridge the gap between the public, scientists, and local governments, fostering a more integrated approach to volcanic studies.

To further investigate Irazú's volcanic activity innovative approaches and methodologies are suggested, including analysis of olivine and apatite melt inclusions and isotopic REE analysis from samples specifically within unit D1. Based on the work of Boyce and Hervig (2008), apatite phenocrysts from the 1963 and 1723 eruptions were examined via secondary ion mass spectrometry to measure the content of volatile elements H, Cl, and F. Additionally, isotopic analysis of $^{206}Pb/^{204}Pb$ could provide valuable insights into the incorporation of mafic forearc crust into the mantle wedge via subduction erosion, as suggested by Goss and Key (2006). These advanced techniques would contribute to a more comprehensive understanding of the volcanic processes at Irazú.

4.4 Summary and conclusions

The geochemical analysis of volcanic material from Irazú Volcano in Costa Rica reveals a complex volcanic system strongly influenced by recent subduction-related fluids. Elevated ratios of fluid mobile elements like Ba/Th, Ba/Nb, and La/Yb indicate significant interaction with fluids from the subducting slab and recharging the shallow magma chamber at intervals of ~500-700 years. Samples over the last ~2400 years show the frequent occurrence of recharge events resulting in the varying influence levels from these fluids, with a notable enrichment of Ba in the 1723 eruption (unit A1). A distinct spike in mafic material around 700 CE is attributed to the recycling process of crystalline mushes in response to eruptive disturbance.

This study also examines the temporal variations of major and minor wt. % oxides based on their stratigraphic positions. The most significant changes are observed in MgO, which shows notable enrichment around 700 and ~1000 CE, preceded by periods of depletion accompanied by increased CaO levels. Calcium oxides also display distinct cycles, with successive increases of 2-3 wt. % followed by average depletions of 3 wt. %. These cycles include notable points of depletion, particularly before unit D1 and in unit C2 (~1420 CE). Typically, such enrichment in MgO and CaO would indicate a less evolved mantle source, but the shallow depth of Irazú’s magma chamber suggests that these elements' fluctuations are due to the disruption of a crystal-liquid network encasing the magma chamber.

The enrichment of TiO2 around unit C2 (~1420 CE) and another unit dated to around 1300 CE coincides with the accumulation of titanium-bearing minerals like ilmenite. Additionally, total alkali concentrations (Na2O+K2O) show five notable peaks around 6 wt. %, interspersed with depleted periods (~4 wt. %). These oscillations, along with elevated Pearce element ratios, indicate the accumulation of plagioclase along the chamber walls. This pattern suggests that the composition changes result from the interaction between the newer melt influx and the existing cumulate lining in the magma chamber, rather than direct crystallization processes.

REFERENCES

Alvarado, G. E., Carr, M. J., Turrin, B. D., Swisher, C. C., Schmincke, H. U., & Hudnut, K. W. (2006). Recent volcanic history of Irazú volcano, Costa Rica: Alternation and mixing of two magma batches, and pervasive mixing.

Alvarado, G. (2011). Los volcanes de Costa Rica: geología, historia, riqueza natural y su gente. San José. EUNED: Costa Rica.

Alvarado, G. E., Campos-Duran, D., Brenes-André, J., Alpízar, Y., Núñez, S., Esquivel, L., Sibaja, J., Fallas, B. (2020). Volcanic Hazards of Irazú.

Alvarado, G. E., & Schmincke, H. U. (2013). The 1723 AD violent strombolian and phreatomagmatic eruption at Irazú Volcano, Costa Rica. Revista Geológica de América Central, (48), 41-61.

Alvarado, G. E. (1993). Volcanology and Petrology of Irazú Volcano, Costa Rica (Doctoral dissertation, Christian-Albrechts-Universität zu Kiel $ f.).

Astorga, A. Análisis de Alcance Ambiental del Plan GAM; Parte II. Technical report, PRUGAM, San José, Costa Rica, 2008.

Armbrister T. The sky is falling. Saturday Evening Post, 237(20), 1964.

Boyce, J. W., & Hervig, R. L. (2009). Apatite as a monitor of late-stage magmatic processes at Volcán Irazú, Costa Rica. Contributions to Mineralogy and Petrology, 157, 135-145.

Benjamin, E. R., Plank, T., Wade, J. A., Kelley, K. A., Hauri, E. H., & Alvarado, G. E. (2007). High water contents in basaltic magmas from Irazú Volcano, Costa Rica. Journal of Volcanology and Geothermal Research, 168(1-4), 68-92.

Brinkhoff, T. (2020). COSTA RICA: Administrative Division Cantons and Districts. City Population. Retrieved November 27, 2022, from http://www.citypopulation.de/en/costarica/admin/

Campos-Durán, D., Alvarado, G. E., & Martí, J. (2024). Upper Holocene tephro-chronostratigraphy of Irazú Volcano, Costa Rica. Scientific reports, 14(1), 7100.

Clark, S. K. The recent eruptive history of Irazú volcano, Costa Rica: A study of the tephra deposits of the last 2500 years with geochemical and isotopic analysis of the 1963–1965 eruption. (M.Sc. Tesis). Univ. Iowa (1993).

Clark, S. K., Reagan, M. K., & Plank, T. (1998). Trace element and U-series systematics for 1963-1965 tephras from Irazú volcano, Costa Rica: Implications for magma generation processes and transit times. Geochimica et cosmochimica acta, 62(15), 2689-2699.

Clark, S. K., Reagan, M. K., & Trimble, D. A. (2006). Tephra deposits for the past 2600 years from Irazú volcano, Costa Rica.

Clark, S. K., Reagan, M. K., & Trimble, D. A. (1994). Recent tephra stratigraphy and implications for future hazards at Irazu Volcano, Costa Rica. In Abstracts with programs-Geological Society of America (Vol. 26, No. 2, p. 45). Geological Society of America (GSA).

Carr, M. J., & Walker, J. A. (1987). Intra-eruption changes in composition of some mafic to intermediate tephras in Central America. Journal of Volcanology and Geothermal Research, 33(1-3), 147-159.

Carr, M. J., Patino, L. C., & Feigenson, M. D. (2007). Petrology and geochemistry of lavas. Central America: geology, resources and hazards, 1, 565-577.

Carr, M. J., Saginor, I., Alvarado, G. E., Bolge, L. L., Lindsay, F. N., Milidakis, K., ... & Swisher III, C. C. (2007). Element fluxes from the volcanic front of Nicaragua and Costa Rica. Geochemistry, Geophysics, Geosystems, 8(6).

Castillo, G. B., Núñez, S., & Malavassi, E. (2018). Ash fallout hazard from Irazú volcano, Costa Rica. Revista Geográfica de Chile Terra Australis, 54(1), 13-25.

Defant, M. J., & Drummond, M. S. (1990). Derivation of some modern arc magmas by melting of young subducted lithosphere. nature, 347(6294), 662-665.

Epiard, M., Avard, G., De Moor, J. M., Martínez Cruz, M., Barrantes Castillo, G., & Bakkar, H. (2017). Relationship between diffuse CO2 degassing and volcanic activity. Case study of the Poás, Irazú, and Turrialba Volcanoes, Costa Rica. Frontiers in Earth Science, 5, 71.

Goss, A. R., & Kay, S. M. (2006). Steep REE patterns and enriched Pb isotopes in southern Central American arc magmas: Evidence for forearc subduction erosion?. Geochemistry, Geophysics, Geosystems, 7(5).

Hayes, J. L., Holbrook, W. S., Lizarralde, D., Van Avendonk, H. J., Bullock, A. D., Mora, M., ... & Ramírez, C. (2013). Crustal structure across the Costa Rican volcanic arc. Geochemistry, Geophysics, Geosystems, 14(4), 1087-1103.

Hebert, L. B., Asimow, P., & Antoshechkina, P. (2009). Fluid source-based modeling of melt initiation within the subduction zone mantle wedge: Implications for geochemical trends in arc lavas. Chemical Geology, 266(3-4), 297-310.

Kruger, W., Latypov, R. In situ crystallization of non-cotectic and foliated igneous rocks on a magma chamber floor. *Commun Earth Environ* **3**, 251 (2022). https://doi.org/10.1038/s43247-022-00584-6

Lemieux, G. H. (1977). Human responses and adjustments to the 1963-65 ashfalls of Irazu volcano, Costa Rica: a geographical study of environmental perception. Revista Geográfica, (86/87), 227-274.

McDonough WF, Sun SS (1995) The composition of the Earth. Chem Geol 120:223–253

Montero Pohly, W. (1989). Sismicidad Histórica de Costa Rica. Geofisica Internacional, 28(3), 531-559.

Montero, W., & Alvarado, G. E. (1995). El terremoto de Patillos del 30 de diciembre de 1952 (Ms= 5, 9) y el contexto neotectónico de la región del volcán Irazú, Costa Rica. Revista Geológica de América Central, 18

Montero P, W., & Dewey, J. W. (1982). Shallow-focus seismicity, composite focal mechanism, and tectonics of the Valle Central of Costa Rica. Bulletin of the Seismological Society of America, 72(5), 1611-1626.

Murata, K. J., Dondoli, C., & Sáenz, R. (1966). The 1963–65 eruption of Irazu volcano, Costa Rica (the period of March 1963 to October 1964). Bulletin Volcanologique, 29, 763-793.

Oeser, M., Ruprecht, P., & Weyer, S. (2018). Combined Fe-Mg chemical and isotopic zoning in olivine constraining magma mixing-to-eruption timescales for the continental arc volcano Irazú (Costa Rica) and Cr diffusion in olivine. American Mineralogist, 103(4), 582-599.

Pearce, J. A., & Peate, D. W. (1995). "Tectonic implications of the composition of volcanic arc magmas." Annual Review of Earth and Planetary Sciences, 23(1), 251-285.

Pavanelli, N., Capaccioni, B., Sarocchi, D., Duarte, E., Vaselli, O., Tassi, F., & Calderoni, G. (2004). Geology and Stability of the Southern Flank of Irazu Volcano (Costa Rica). Geology and Stability of the Southern Flank of Irazu Volcano (Costa Rica), 1000-1007.

Pérez-Umaña, D., Quesada-Román, A., & Tefogoum, G. Z. (2020). Geomorphological heritage inventory of Irazú volcano, Costa Rica. International Journal of Geoheritage and Parks, 8(1), 31-47.

Pirulli, M., & Mora, R. (2017). Numerical Analysis of a Potential Debris Flow Event on the Irazú Volcano, Costa Rica. In Advancing Culture of Living with Landslides: Volume 5 Landslides in Different Environments (pp. 89-100). Springer International Publishing.

Popa, R. G., Bachmann, O., & Huber, C. (2021). Explosive or effusive style of volcanic eruption determined by magma storage conditions. Nature Geoscience, 14(10), 781-786.

Rollinson, H. (1993). "Using Geochemical Data: Evaluation, Presentation, Interpretation."

Rouwet, D., Mora-Amador, R., Ramírez-Umaña, C., & González, G. (2010). Hydrogeochemical model of the Irazú and Turrialba` `twin volcanoes"(Costa Rica). In AGU Fall Meeting Abstracts (Vol. 2010, pp. V23A-2392).

Rouwet, D., Mora-Amador, R., Ramirez, C., Gonzalez, G., Baldoni, E., Pecoraino, G., ... & Tranne, C. A. (2021). Response of a hydrothermal system to escalating phreatic unrest: the case of Turrialba and Irazú in Costa Rica (2007–2012). Earth, Planets and Space, 73, 1-26.

Siebert, L., Cottrell, E., Venzke, E., Edwards, B., 2013. Catalog of earth's documented Holocene eruptions. In: The Encyclopedia of Volcanoes, Sigurdsson ed., Appendix 2, pp. 1367–1400.

Tatsumi, Y., & Eggins, S. (1995). "Subduction Zone Magmatism."

The Nature Conservancy. (n.d.). Water blueprint: San Jose, Costa Rica. The Nature Conservancy. Retrieved June 11, 2024, from https://water.nature.org/waterblueprint/city/san_jose_cri/#/c=10:9.69495:-83.85411

Thompson, R. N., & Morrison, M. A. (1988). "Asthenospheric and lower-lithospheric sources for alkaline basalts: evidence from the Tertiary basalts of southern Scotland." Contributions to Mineralogy and Petrology, 100(4), 483-497.

Ulate, C. A., & Corrales, M. F. (1966). Mud floods related to the Irazu volcano eruptions. Journal of the Hydraulics Division, 92(6), 117-129.

Villegas A, R. J., Petrinovic, I. A., & Carniel, R. (2019). S-wave velocity zones at the Irazú Volcano (Costa Rica). Journal of South American Earth Sciences, 90, 314-324.

Vaselli, O., Tassi, F., Duarte, E., Fernandez, E., Poreda, R. J., & Huertas, A. D. (2010). Evolution of fluid geochemistry at the Turrialba volcano (Costa Rica) from 1998 to 2008. Bulletin of Volcanology, 72, 397-410.

Waldron, H. H. (1967). Debris flow and erosion control problems caused by the ash eruptions of Irazú Volcano, Costa Rica (No. 1241-I). 1-37.

Winter, J. D. (2001). An introduction to igneous and metamorphic petrology.

APPENDICES

Appendix A: Complete geochemical results including major and minor wt. %, and trace element (ppm) concentrations from samples collected for this study. This includes significant tephra layers.

CE	6024-5912 BCE			450	460	500	540	540	~580
Unit ID	SSC			E1	E2	E4	E5	E5	
Samples	Pl1	Pl3	Pi2	CV2	CV3A	CV3B	CV4	CV6	CV7
Stratigraphy	1	1	1.5	5	5.5	6	6.5	6.5	7
SiO2	55.27	53.29	57.92	56.28	55.09	55.36	53.54	53.34	52.56
Al2O3	18.45	18.99	17.31	18.10	17.94	18.53	18.04	18.37	17.98
CaO	7.61	7.83	6.86	7.14	7.34	7.03	8.20	8.36	8.68
TiO2	0.81	0.97	0.83	0.96	1.07	1.04	1.01	1.08	1.07
K2O	1.80	2.04	1.82	2.07	2.12	1.95	1.92	1.80	1.84
MnO	0.12	0.14	0.11	0.12	0.14	0.13	0.13	0.13	0.14
Fe2O3	7.29	8.42	6.88	7.31	7.80	8.00	8.13	8.22	8.83
Na2O	3.77	3.76	2.66	3.55	3.71	3.29	3.49	3.26	3.39
MgO	4.63	4.29	5.29	4.17	4.43	4.35	5.24	5.10	5.24
P2O5	0.25	0.26	0.31	0.29	0.37	0.32	0.30	0.33	0.27
TOTALS	100.00	100.00	100.00	100.00	100.00	100.00	100.00	100.00	100.00
Sc	24.62	18.81	18.41	21.69	17.34	17.06	21.41	19.75	20.14
V	254.74	192.18	240.97	234.46	178.30	174.57	201.40	275.02	297.71
Cr	87.45	51.86	179.79	67.10	70.46	91.28	100.97	141.37	108.03
Mn	1177.13	912.97	735.89	1128.91	912.84	883.76	921.07	1069.62	1215.79
Co	30.59	23.84	18.86	27.77	25.61	25.60	24.99	27.70	30.67
Cu	95.85	136.28	72.13	102.70	56.72	119.38	73.64	124.05	132.63
Zn	72.86	108.20	55.51	96.87	53.37	79.76	64.80	88.99	102.77
Ga	26.62	20.29	17.83	23.59	18.32	19.18	19.22	20.85	23.00
As	4.53	3.31	4.75	4.47	3.99	3.56	3.21	3.09	3.25

Rb	57.92	47.98	69.90	68.12	53.74	47.75	46.84	52.01	53.16
Sr	1193.30	812.54	1007.01	1101.61	846.65	946.24	867.49	1116.14	1159.19
Y	21.49	16.70	22.74	23.22	20.55	19.66	17.15	22.42	23.22
Zr	184.17	145.10	211.72	206.08	191.92	185.68	155.35	176.87	176.24
Nb	18.65	12.52	11.99	21.16	22.28	20.85	15.42	24.17	22.55
Mo	2.89	1.35	3.19	2.90	2.41	2.57	1.08	2.02	2.12
Sn	2.57	3.54	0.86	1.09	1.07	0.65	0.69	0.32	0.39
Cs	0.44	0.63	0.64	0.83	0.64	0.42	0.54	0.40	0.46
Ba	913.25	707.61	1045.07	907.70	730.66	717.63	709.16	777.20	849.85
La	41.52	29.84	51.91	45.43	42.72	39.62	35.14	46.56	44.52
Ce	82.02	57.77	111.93	91.06	83.69	82.16	70.70	92.40	88.08
Nd	35.37	26.33	42.81	36.69	33.45	34.50	30.32	38.02	37.20
Sm	6.61	4.99	7.73	7.00	6.23	7.09	5.35	7.38	7.20
Eu	1.89	1.34	2.17	1.96	1.64	1.84	1.56	2.05	2.08
Gd	5.12	4.01	6.17	5.25	4.75	5.24	4.59	5.34	5.47
Dy	4.41	3.32	4.39	4.27	3.80	4.11	3.55	4.36	4.43
Ho	0.78	0.57	0.74	0.74	0.68	0.71	0.61	0.75	0.78
Er	2.18	1.44	2.11	1.76	2.06	2.15	1.41	2.15	2.27
Yb	1.95	1.54	1.99	2.07	1.63	1.88	1.55	1.88	1.91
Lu	0.28	0.20	0.26	0.28	0.24	0.27	0.22	0.25	0.29
Hf	4.61	3.39	4.30	4.64	4.43	4.50	3.61	4.47	4.66
Ta	1.07	0.63	1.03	1.18	1.26	1.15	0.88	1.34	1.27
Pb	9.56	4.18	6.61	5.52	6.21	7.23	4.23	5.70	5.92
Th	9.33	7.41	12.09	11.01	9.73	9.91	8.49	9.95	9.50
U	3.34	2.65	4.25	3.87	3.26	3.51	2.82	3.30	3.40
CE	>700	>700	>700	>700	700	700	700	700	700
Unit ID					D1	D1	D1	D1	D1
Samples	PR13	PR12	PR11	PR9B	PR7A	PR7D	PR7E	PR7G	PR7H
Stratigraphy	8	8.5	9	10	11	11	11	11	11
SiO2	54.61	54.82	54.70	54.42	49.65	51.71	51.36	50.60	51.96

Al2O3	17.09	19.56	18.65	17.74	15.56	16.03	15.43	16.80	16.88
CaO	9.30	7.07	7.27	7.86	9.39	8.79	8.95	9.22	8.71
TiO2	0.70	1.06	1.11	0.87	1.09	1.17	1.19	1.20	1.14
K2O	1.34	1.67	2.08	2.07	1.50	1.60	1.58	1.78	1.54
MnO	0.17	0.12	0.13	0.12	0.14	0.14	0.16	0.15	0.13
Fe2O3	9.17	7.81	8.29	7.56	8.88	8.95	9.31	9.06	8.65
Na2O	3.00	3.50	3.62	3.74	2.83	3.19	2.97	3.33	2.79
MgO	4.49	4.07	3.85	5.33	10.62	8.06	8.73	7.51	7.84
P2O5	0.14	0.32	0.29	0.27	0.33	0.35	0.34	0.38	0.36
TOTALS	100.00	100.00	100.00	100.00	99.99	100.00	100.02	100.00	100.00
Sc	23.36	19.68	14.51	20.47	25.57	18.96	27.59	25.02	22.37
V	244.31	190.13	175.93	231.19	199.36	191.26	221.33	203.61	185.37
Cr	80.20	69.36	53.85	163.99	365.68	256.95	242.24	248.83	309.27
Mn	1087.43	847.53	784.16	1081.54	1096.70	1031.96	1219.15	1047.24	1049.92
Co	26.52	22.89	19.17	28.53	37.47	32.58	40.25	34.44	34.23
Cu	80.45	73.51	67.37	70.96	56.81	56.48	74.64	97.09	72.79
Zn	68.74	87.98	53.40	62.92	62.14	54.99	70.96	78.69	60.03
Ga	24.41	21.95	20.82	24.84	18.83	19.60	19.66	22.61	21.04
As	4.18	4.19	5.30	5.09	2.71	3.33	2.66	4.16	3.85
Rb	70.48	46.48	51.74	70.13	43.78	44.57	43.22	47.11	43.03
Sr	1191.45	930.05	901.60	1065.63	859.97	988.36	915.90	1015.24	920.03
Y	24.60	20.45	18.73	22.62	22.59	21.04	19.88	22.53	21.06
Zr	230.18	194.45	207.08	216.41	166.34	179.71	165.57	180.93	183.73
Nb	22.89	21.59	19.02	19.96	24.10	27.10	25.54	28.78	24.72
Mo	2.97	5.45	2.98	3.33	3.48	2.01	0.97	0.95	2.30
Sn	1.09	1.09	1.03	1.13	0.81	1.01	0.75	1.07	1.03
Cs	0.84	0.44	0.87	1.14	0.32	0.61	0.45	0.54	0.56
Ba	1028.78	851.01	941.74	975.42	637.10	742.72	668.31	745.39	694.98
La	50.16	42.48	43.37	44.89	41.54	46.93	42.23	47.59	44.06
Ce	104.11	78.15	85.78	83.85	78.26	96.97	86.00	98.89	91.56
Nd	41.80	33.66	35.47	37.99	35.66	41.70	36.58	42.27	37.71

Sm	7.96	6.30	6.52	7.41	6.87	8.01	6.85	7.43	7.41
Eu	2.15	1.71	1.87	2.07	1.83	2.35	1.92	2.10	2.02
Gd	5.99	4.81	5.08	5.91	5.33	6.20	5.83	5.87	5.69
Dy	4.82	3.85	3.94	4.70	4.12	4.59	4.25	4.55	4.39
Ho	0.82	0.64	0.66	0.77	0.69	0.74	0.71	0.77	0.72
Er	2.64	1.35	2.09	2.50	1.43	2.24	1.58	1.82	2.25
Yb	2.08	1.65	1.84	2.18	1.63	1.82	1.69	1.82	1.81
Lu	0.29	0.24	0.26	0.31	0.24	0.25	0.24	0.24	0.25
Hf	5.59	4.44	5.37	5.68	3.73	4.58	3.68	3.95	4.44
Ta	1.35	1.00	1.22	1.23	1.08	1.61	1.42	1.32	1.41
Pb	7.27	6.33	7.65	7.78	4.24	5.20	2.94	3.81	5.27
Th	12.13	9.11	11.03	12.07	6.74	8.18	7.52	8.14	8.21
U	4.09	3.11	3.91	4.20	2.32	2.78	2.46	2.71	2.67
CE	<700A	<700B	>700	<700	<700	<700	<910A	<1290	1300
Unit ID									
Samples	PR5	PR3	EPN2	EPN5	EPN6	EPN7	EPN8A	ES4	PM1A
Stratigraphy	12	12.5	10	13	14	15	16	17	17.5
SiO2	54.88	54.90	56.80	52.52	53.05	52.83	52.21	51.69	51.60
Al2O3	18.54	18.04	17.55	16.62	16.86	16.97	15.39	16.48	16.54
CaO	7.44	7.60	6.71	8.91	8.64	8.60	9.82	9.05	8.63
TiO2	1.07	1.01	0.93	1.16	0.98	1.04	0.96	1.14	2.14
K2O	1.91	2.19	2.24	2.17	1.86	1.82	1.49	1.43	1.61
MnO	0.13	0.14	0.13	0.15	0.15	0.14	0.17	0.16	0.15
Fe2O3	7.91	7.91	7.83	9.19	8.96	8.99	9.45	9.86	10.49
Na2O	3.80	3.80	3.36	3.81	3.32	3.33	2.82	3.06	3.07
MgO	4.03	4.15	4.18	5.16	5.94	6.00	7.47	6.82	5.38
P2O5	0.29	0.27	0.28	0.31	0.24	0.27	0.23	0.31	0.39
TOTALS	100.00	100.00	100.00	100.00	100.00	100.00	100.00	100.00	100.00
Sc	18.93	31.37	24.06	30.46	25.82	27.05	32.02	25.62	21.78
V	205.99	314.29	230.53	289.09	219.35	225.65	239.92	219.90	199.81
Cr	45.14	132.52	60.38	129.99	92.27	157.68	113.42	142.73	141.93

Mn	1018.34	1542.84	1146.30	1615.68	1038.76	1046.22	1319.52	1072.49	1030.41
Co	24.84	39.09	27.39	38.31	28.81	29.60	35.23	31.64	32.27
Cu	97.71	117.40	89.65	100.70	76.71	102.88	83.26	57.99	164.17
Zn	63.86	99.17	113.59	92.88	86.79	88.62	79.23	72.11	106.77
Ga	22.61	35.92	25.23	33.13	19.73	21.18	18.99	19.19	19.02
As	3.04	7.76	4.52	6.09	3.97	3.36	2.07	2.76	3.17
Rb	51.24	83.09	73.86	80.64	48.50	49.74	40.31	37.58	42.28
Sr	960.05	1321.76	996.10	1440.36	856.41	911.07	847.09	861.33	860.87
Y	19.46	31.07	20.89	28.65	18.97	18.56	19.37	19.31	27.35
Zr	178.83	279.06	219.38	267.16	150.87	161.89	131.32	144.30	226.62
Nb	18.46	32.57	21.03	32.01	14.20	15.81	14.01	16.20	38.55
Mo	1.73	3.97	2.82	4.24	1.38	1.41	0.72	3.01	1.55
Sn	0.68	1.46	1.33	1.35	0.67	0.89	0.54	0.83	1.22
Cs	0.65	0.63	1.15	1.01	0.59	0.75	0.43	0.29	0.56
Ba	799.78	1156.91	929.16	1087.39	739.67	707.37	614.43	588.54	575.25
La	39.37	57.67	44.31	63.14	36.05	34.30	31.53	31.77	45.53
Ce	78.90	117.87	81.38	122.40	70.21	69.65	62.83	60.51	95.96
Nd	32.57	49.84	34.88	50.86	31.43	31.33	29.01	27.30	45.21
Sm	6.16	9.08	6.75	9.65	5.73	5.89	5.49	5.45	9.53
Eu	1.66	2.56	1.75	2.66	1.60	1.64	1.59	1.50	2.67
Gd	5.12	6.84	5.16	7.34	4.66	5.20	4.96	4.35	7.07
Dy	3.81	5.81	4.18	5.97	3.83	4.17	3.98	3.63	5.44
Ho	0.68	1.03	0.75	0.96	0.67	0.72	0.68	0.58	0.94
Er	1.52	2.85	2.30	3.09	1.69	1.95	1.57	1.28	2.72
Yb	1.71	2.57	2.10	2.55	1.73	1.84	1.70	1.47	2.09
Lu	0.25	0.37	0.31	0.36	0.23	0.24	0.24	0.22	0.29
Hf	3.86	6.61	5.15	6.45	3.38	3.70	2.95	3.42	5.15
Ta	1.05	1.80	1.43	1.88	0.87	1.37	0.79	0.79	2.26
Pb	4.27	9.50	7.20	8.50	4.35	3.24	3.11	4.46	3.56
Th	9.35	13.48	12.12	13.12	8.33	7.84	6.71	6.29	6.91
U	3.15	4.79	4.16	4.35	2.78	2.78	2.19	2.13	2.45

CE	1420	<1510	<1610	<1610	1963-1965				
Unit ID	C2				A4	A4	A4	A4	A4
Samples	PD1A	PD2A	ES5	ES6	PD3	PM4A	PM4B	PM5A	PM5B
Stratigraphy	18	19	22	22	26	26	26	26	26
SiO2	53.43	53.84	54.73	53.27	54.15	52.94	53.46	53.08	53.53
Al2O3	17.10	17.83	18.51	15.49	18.12	17.82	17.49	15.84	15.75
CaO	5.40	7.85	7.64	8.11	7.99	9.23	8.81	8.86	8.52
TiO2	1.99	0.88	0.90	1.30	0.94	1.23	1.16	1.02	1.15
K2O	2.92	2.05	2.05	2.10	2.11	2.20	2.22	2.23	2.49
MnO	1.20	0.13	0.13	0.14	0.12	0.14	0.14	0.15	0.14
Fe2O3	9.70	8.39	7.67	8.67	7.86	8.13	8.16	8.75	8.82
Na2O	7.69	3.96	3.53	3.62	3.75	3.29	3.56	3.61	3.62
MgO	0.15	4.80	4.51	6.89	4.66	4.68	4.67	6.21	5.70
P2O5	0.40	0.27	0.34	0.42	0.30	0.34	0.33	0.26	0.30
TOTALS	100.00	100.00	100.00	100.00	100.00	100.00	100.00	100.00	100.00
Sc	22.38	19.93	20.90	25.20	27.12	22.73	16.65	25.15	23.51
V	298.01	171.57	178.84	210.06	283.56	225.84	189.66	190.10	190.28
Cr	225.87	121.25	98.67	262.15	102.74	73.94	67.39	132.99	108.43
Mn	1070.23	554.28	917.83	1232.28	1314.65	1035.80	890.24	992.17	1008.80
Co	37.94	22.21	23.02	37.69	34.88	24.40	22.01	26.54	24.59
Cu	268.06	85.89	108.62	70.06	164.04	118.92	133.64	74.68	64.42
Zn	87.52	62.54	99.37	88.70	111.60	99.41	86.26	73.18	66.37
Ga	25.14	20.54	19.12	25.82	28.69	20.86	20.36	19.17	18.14
As	5.47	4.39	2.95	3.50	4.51	2.98	3.76	3.14	2.99
Rb	42.31	52.94	53.77	67.30	78.89	59.47	48.66	59.31	65.70
Sr	1094.71	791.72	805.85	1101.32	1388.80	868.76	748.11	792.30	771.21
Y	39.02	17.01	20.72	25.77	27.69	25.47	24.48	24.26	25.57
Zr	307.70	277.95	178.88	271.90	245.63	205.96	183.06	191.72	209.29
Nb	32.87	9.52	17.31	35.66	25.23	18.79	21.04	18.53	21.26
Mo	2.68	3.00	1.70	1.87	3.23	1.63	2.80	1.26	1.84
Sn	6.08	1.20	0.80	1.08	4.52	1.08	0.98	0.67	0.80

Cs	0.42	0.46	0.63	0.61	0.89	0.75	0.67	0.69	0.73
Ba	889.57	726.04	668.93	899.84	1054.07	861.61	687.58	736.78	778.72
La	73.45	31.41	35.77	66.09	60.05	48.43	44.01	42.33	46.83
Ce	170.63	76.32	69.01	136.17	122.04	102.59	82.61	83.05	88.42
Nd	73.72	26.74	29.80	51.63	48.97	43.76	37.73	37.05	38.49
Sm	13.99	4.92	5.93	8.94	9.12	8.03	7.39	6.86	7.66
Eu	4.07	1.34	1.53	2.55	2.46	2.18	2.05	1.77	1.96
Gd	11.69	4.10	4.44	7.45	6.68	6.33	5.71	5.46	5.86
Dy	8.21	3.12	3.74	5.58	5.37	5.35	4.64	4.63	4.84
Ho	1.36	0.58	0.67	0.89	0.92	0.91	0.78	0.79	0.82
Er	3.63	1.74	1.57	2.04	2.15	2.52	2.07	2.01	1.92
Yb	3.05	1.50	1.69	2.26	2.38	2.30	2.08	2.06	2.05
Lu	0.38	0.23	0.24	0.31	0.35	0.33	0.35	0.29	0.30
Hf	5.78	5.96	4.01	5.84	5.73	4.54	3.81	4.24	4.60
Ta	2.86	1.09	1.58	2.05	1.51	1.04	1.05	0.87	1.14
Pb	5.40	6.03	5.13	5.20	6.63	3.01	2.99	4.02	4.43
Th	8.45	10.21	9.14	12.84	13.33	9.37	8.37	9.76	10.70
U	3.07	3.42	3.13	3.91	4.67	3.18	3.03	3.41	3.71
CE	1480	1640	1640						
Unit ID	ECC								
Samples	CL1A	CL2	CL3	Tj1sc	Tr2				
Stratigraphy	18.5	23	23	23	23				
SiO2	54.74	54.37	53.61	54.56	53.91				
Al2O3	17.88	17.15	18.33	17.84	17.77				
CaO	8.19	7.52	7.76	8.06	8.60				
TiO2	0.92	1.07	0.99	0.99	1.02				
K2O	2.00	1.68	2.16	1.76	1.76				
MnO	0.13	0.14	0.14	0.13	0.14				
Fe2O3	7.58	8.95	8.07	7.97	8.13				
Na2O	3.51	2.91	3.94	3.47	3.30				
MgO	4.82	5.90	4.72	4.96	5.11				

P2O5	0.23	0.30	0.29	0.26	0.25
TOTALS	100.00	100.00	100.00	100.00	100.00
Sc	22.11	30.27	34.46	22.23	21.83
V	194.55	303.53	341.62	215.89	208.21
Cr	101.15	211.40	126.54	62.31	63.13
Mn	945.69	1257.74	1581.58	1038.81	961.67
Co	23.97	37.90	41.34	26.23	25.32
Cu	92.88	74.55	131.13	129.37	133.76
Zn	81.15	79.42	93.23	79.90	131.75
Ga	18.02	26.12	36.01	18.60	20.90
As	2.73	5.42	6.82	2.49	3.39
Rb	53.81	56.13	82.64	47.73	47.74
Sr	861.72	1041.78	1406.59	1000.38	935.04
Y	19.88	22.69	31.97	19.97	17.81
Zr	173.04	205.99	293.54	148.90	218.63
Nb	16.50	23.95	31.22	15.79	16.87
Mo	1.72	2.75	3.71	1.45	2.27
Sn	0.80	1.13	1.52	0.72	1.20
Cs	0.80	0.45	0.66	0.55	0.59
Ba	715.32	880.08	1240.95	718.66	710.95
La	37.11	44.21	68.60	37.09	33.24
Ce	65.01	86.76	134.48	68.88	64.28
Nd	29.10	37.28	57.47	31.35	28.21
Sm	5.69	7.10	10.56	6.20	5.33
Eu	1.57	2.04	2.97	1.67	1.48
Gd	4.39	5.45	7.93	4.75	4.40
Dy	3.62	4.68	6.37	3.86	3.55
Ho	0.65	0.81	1.09	0.65	0.63
Er	2.06	2.33	2.97	1.52	1.51
Yb	1.78	2.14	2.67	1.68	1.62
Lu	0.26	0.30	0.37	0.23	0.24

Hf	4.03	5.08	6.83	3.25	6.04
Ta	1.27	1.36	1.70	0.86	0.88
Pb	4.49	6.98	9.26	4.22	7.04
Th	8.23	10.00	14.23	7.52	7.21
U	2.80	3.39	4.99	2.26	2.41

Appendix A1: Trace element ratios (ppm) of key stratigraphic units.

Unit ID	E1	E2	E4	E5	E5	D1	D1	D1	D1	D1	C2
Samples	CV2	CV3A	CV3B	CV4	CV6	PR7A	PR7D	PR7E	PR7G	PR7H	PD1A
Dy/Yb	2.07	2.33	2.18	2.28	2.32	2.52	2.52	2.51	2.50	2.42	2.69
La/Sm	6.49	6.86	5.59	6.56	6.31	6.05	5.86	6.17	6.41	5.95	5.25
Th/Yb	5.33	5.97	5.27	5.47	5.29	4.12	4.50	4.44	4.48	4.52	2.77
Zr/Ti	215.62	178.55	177.72	154.48	164.11	152.61	153.78	139.13	151.30	160.64	17.99
Sr/Sm	157.38	135.99	133.44	162.04	151.26	125.15	123.39	133.80	136.73	124.17	78.26
Zr/Hf	44.38	43.29	41.26	43.01	39.53	44.60	39.22	45.03	45.77	41.34	53.24
Th/La	0.24	0.23	0.25	0.24	0.21	0.16	0.17	0.18	0.17	0.19	0.11
Zr/Y	8.87	9.34	9.45	9.06	7.89	7.36	8.54	8.33	8.03	8.72	7.89
Nb/Y	0.91	1.08	1.06	0.90	1.08	1.07	1.29	1.29	1.28	1.17	0.84
Hf/Y	0.20	0.22	0.23	0.21	0.20	0.17	0.22	0.18	0.18	0.21	0.15
Ba/Th	82.44	75.06	72.40	83.48	78.13	94.58	90.84	88.87	91.57	84.66	105.31
Ce/Th	8.27	8.60	8.29	8.32	9.29	11.62	11.86	11.44	12.15	11.15	20.20
La/Nb	2.15	1.92	1.90	2.28	1.93	1.72	1.73	1.65	1.65	1.78	2.23
La/Yb	22.00	26.19	21.05	22.62	24.77	25.41	25.82	24.94	26.19	24.28	24.09
Ce/Yb	44.09	51.30	43.65	45.51	49.16	47.87	53.36	50.79	54.42	50.45	55.95
Zr/Nb	9.74	8.61	8.90	10.08	7.32	6.90	6.63	6.48	6.29	7.43	9.36
Zr/Th	18.72	19.72	18.73	18.29	17.78	24.70	21.98	22.02	22.23	22.38	36.43
Nb/U	5.46	6.84	5.94	5.46	7.33	10.37	9.76	10.40	10.63	9.27	10.72
Ba/La	19.98	17.10	18.11	20.18	16.69	15.34	15.83	15.83	15.66	15.77	1.16
Sr/Y	47.43	41.21	48.14	50.59	49.78	38.07	46.97	46.07	45.06	43.68	0.15
Ba/Th	82.44	75.06	72.40	83.48	78.13	94.58	90.84	88.87	91.57	84.66	49.44
U/La	0.09	0.08	0.09	0.08	0.07	0.06	0.06	0.06	0.06	0.06	0.94
U/Th	0.35	0.33	0.35	0.33	0.33	0.35	0.34	0.33	0.33	0.32	3.20
La/Yb	22.00	26.19	21.05	22.62	24.77	25.41	25.82	24.94	26.19	24.28	641.07

Ba/Sr	0.82	0.86	0.76	0.82	0.70	0.74	0.75	0.73	0.73	0.76	1.77
Zr/Nb	9.74	8.61	8.90	10.08	7.32	6.90	6.63	6.48	6.29	7.43	4.83
Nb/Ta	17.89	17.65	18.09	17.45	17.99	22.35	16.83	17.97	21.84	17.55	78.89
CaO/Al2O3	0.39	0.41	0.38	0.45	0.46	0.60	0.55	0.58	0.55	0.52	0.08
Nb/Zr	0.10	0.12	0.11	0.10	0.14	0.14	0.15	0.15	0.16	0.13	0.07
Th/Yb	5.33	5.97	5.27	5.47	5.29	4.12	4.50	4.44	4.48	4.52	1.63
Ta/Yb	0.57	0.77	0.61	0.57	0.71	0.66	0.89	0.84	0.73	0.78	0.13
La/Nd	1.24	1.28	1.15	1.16	1.22	1.17	1.13	1.15	1.13	1.17	0.01

Unit ID	A4					ECC					SSC		
Samples	PD3	PM4A	PM4B	PM5A	PM5B	CL1A	CL2	CL3	Tj1sc	Tr2	Pl1	Pl3	Pi2
Dy/Yb	2.26	17.79	15.62	17.40	16.63	2.03	2.18	2.39	2.31	2.19	2.27	2.16	2.21
La/Sm	6.59	34.11	30.56	32.65	30.16	6.52	6.23	6.50	5.98	6.24	6.29	5.98	6.72
Th/Yb	5.60	91.95	82.13	75.46	72.78	4.62	4.67	5.33	4.49	4.46	4.79	4.82	6.09
Zr/Ti	261.14	0.07	0.07	0.08	0.08	188.06	192.31	296.08	150.43	214.42	226.32	149.54	255.72
Sr/Sm	152.33	0.34	0.36	0.35	0.35	151.53	146.78	133.24	161.37	175.40	180.65	162.72	130.33
Zr/Hf	42.85	21.16	20.50	22.82	42.95	40.54	42.96	45.81	36.21	39.94	42.79	49.25	44.05
Th/La	0.22	0.92	0.93	1.01	0.22	0.23	0.21	0.20	0.22	0.22	0.25	0.23	0.19
Zr/Y	8.87	8.70	10.35	9.85	8.71	9.08	9.18	7.46	12.28	8.57	8.69	9.31	8.61
Nb/Y	0.91	20.07	21.30	18.62	0.83	1.06	0.98	0.79	0.95	0.87	0.75	0.53	0.88
Hf/Y	0.21	0.50	0.56	0.54	0.20	0.22	0.21	0.16	0.34	0.21	0.20	0.19	0.20
Ba/Th	79.09	0.11	0.10	0.10	86.89	88.00	87.20	95.53	98.60	97.90	95.46	86.46	91.55
Ce/Th	9.16	4.02	4.73	5.21	7.90	8.67	9.45	9.16	8.92	8.79	7.79	9.26	10.54
La/Nb	2.38	0.50	0.42	0.56	2.25	1.85	2.20	2.35	1.97	2.23	2.38	4.33	2.09
La/Yb	25.23	1.17	1.14	1.22	20.82	20.66	25.70	22.13	20.54	21.34	19.39	26.15	21.79
Ce/Yb	51.27	5.77	5.84	6.10	36.48	40.53	50.39	41.11	39.72	42.15	37.53	56.38	44.60
Zr/Nb	9.74	2.23	2.24	2.36	10.49	8.60	9.40	9.43	12.96	9.87	11.58	17.67	9.78
Zr/Th	18.43	5.96	6.17	6.11	21.02	20.60	20.63	19.79	30.32	19.74	19.58	17.52	24.14
Nb/U	5.40	4.02	4.73	5.21	5.89	7.06	6.26	6.99	7.01	5.58	4.72	2.82	7.02

Ba/La	17.55	101.22	115.46	100.68	19.28	19.90	18.09	19.38	21.39	21.99	23.71	20.13	17.77
Sr/Y	50.15	48.01	45.18	45.50	43.35	45.92	43.99	50.10	52.51	55.52	48.65	44.28	30.52
Ba/Th	79.09	0.19	0.23	0.23	86.89	88.00	87.20	95.53	98.60	97.90	95.46	86.46	91.55
U/La	0.08	7.48	7.90	8.19	0.08	0.08	0.07	0.06	0.07	0.08	0.09	0.08	0.07
U/Th	0.35	0.86	0.76	0.83	0.34	0.34	0.35	0.30	0.33	0.36	0.36	0.35	0.35
La/Yb	25.23	0.16	0.17	0.18	20.82	20.66	25.70	22.13	20.54	21.34	19.39	26.15	21.79
Ba/Sr	0.76	82.13	75.46	72.78	0.83	0.84	0.88	0.72	0.76	0.77	0.87	1.04	1.07
Zr/Nb	9.74	9.87	8.51	8.26	10.49	8.60	9.40	9.43	12.96	9.87	11.58	17.67	9.78
Nb/Ta	16.72	2.09	2.28	2.20	13.00	17.56	18.33	18.44	19.15	17.51	19.75	11.68	19.50
CaO/Al2O3	0.44	21.16	20.50	22.82	0.46	0.44	0.42	0.45	0.48	0.41	0.41	0.40	0.50
Nb/Zr	0.10	39.71	40.22	43.09	0.10	0.12	0.11	0.11	0.08	0.10	0.09	0.06	0.10
Th/Yb	5.60	8.70	10.35	9.85	4.62	4.67	5.33	4.49	4.46	4.79	4.82	6.09	4.23
Ta/Yb	0.63	21.86	19.64	19.56	0.71	0.64	0.64	0.51	0.54	0.55	0.41	0.52	0.54
La/Nd	1.23	6.95	5.44	5.73	1.28	1.19	1.19	1.18	1.18	1.17	1.13	1.21	1.09

Appendix B: Major and minor wt. % oxides of geochemical data incorporated from Alvarado (1993). These tephras are from the 1723 and 1963-1965 eruptions.

CE	1723													
Unit ID	A1	A1	A1											
Samples	ALGI 30	ALGI 31	ALGI 32	ALGI 33	ALGI 34	ALGI 37	ALGI 38	ALGI 39	ALGI 40					
Stratigraphy	24	24	24	24	24	24	24	24	24					
SiO2	53.12	53.48	53.26	53.58	53.80	53.66	53.92	54.63	55.07					
Al2O3	17.48	17.47	17.50	17.49	17.37	17.47	17.19	16.89	17.07					
CaO	8.56	8.59	8.65	8.56	8.53	8.52	8.35	7.81	7.69					
TiO2	1.20	1.19	1.19	1.17	1.16	1.16	1.15	1.13	1.13					
K2O	2.16	2.20	2.20	2.18	2.23	2.25	2.28	2.24	2.29					
MnO	0.14	0.13	0.13	0.13	0.13	0.13	0.13	0.13	0.12					
Fe2O3	9.40	9.12	9.19	9.01	8.93	8.94	9.03	8.95	8.69					
Na2O	2.96	2.94	3.00	2.97	3.01	3.04	3.06	3.09	3.00					
MgO	4.54	4.46	4.45	4.48	4.42	4.41	4.47	4.73	4.53					
P2O5	0.44	0.43	0.42	0.42	0.42	0.42	0.42	0.40	0.42					
TOTALS	100.00	100.00	100.00	100.00	100.00	100.00	100.00	100.00	100.00					
CE	1723													
Unit ID	A1													
Samples	V1	V2	V3	V4	V5	V6								
Stratigraphy	24	24	24	24	24	24								
SiO2	53.96	53.88	53.86	54.06	54.24	54.50								

Al2O3	16.95	16.79	16.76	16.81	16.54	16.59								
CaO	8.84	8.88	8.99	8.81	8.62	8.63								
TiO2	1.17	1.18	1.19	1.18	1.16	1.15								
K2O	2.17	2.14	2.14	2.18	2.26	2.25								
MnO	0.13	0.14	0.13	0.13	0.13	0.13								
Fe2O3	8.26	8.30	8.32	8.22	8.30	8.13								
Na2O	3.40	3.39	3.37	3.42	3.43	3.44								
MgO	4.64	4.82	4.78	4.72	4.88	4.76								
P2O5	0.48	0.48	0.46	0.46	0.45	0.42								
TOTALS	100.00	100.00	100.00	100.00	100.00	100.00								
CE	1963-1965													
Unit ID	A4													
Samples	ALGI lb	Al.GI 2b	ALGI 3	ALGJ 4a	ALGI 5	ALGI 6	ALGI 7b	ALGI 10	ALGI 8a	ALGI 9a	ALGI 9d	ALGI 11c		
Stratigraphy	26	26	26	26	26	26	26	26	26	26	26	26		
SiO2	54.57	54.70	55.04	54.35	54.61	54.88	54.74	54.64	54.59	54.88	54.83	54.97		
Al2O3	16.71	16.54	16.73	16.61	16.62	16.74	16.61	16.69	16.62	16.63	16.73	16.55		
CaO	7.99	7.98	7.73	8.06	7.88	7.85	7.88	7.98	8.06	7.84	7.85	7.81		
TiO2	0.96	0.96	0.96	0.97	0.98	0.94	0.95	0.95	0.94	0.96	0.94	0.96		
K2O	2.03	2.02	2.11	1.95	2.01	1.96	1.99	1.95	1.93	1.99	1.98	2.03		
MnO	0.12	0.12	0.12	0.12	0.12	0.12	0.12	0.12	0.12	0.12	0.12	0.12		
Fe2O3	8.66	8.69	8.59	8.79	8.83	8.54	8.67	8.72	8.63	8.63	8.54	8.67		
Na2O	2.83	2.83	2.96	2.86	2.87	2.91	2.88	2.83	2.86	2.93	2.94	2.94		
MgO	5.80	5.83	5.45	5.98	5.76	5.74	5.83	5.82	5.96	5.70	5.74	5.64		
P2O5	0.33	0.32	0.32	0.31	0.32	0.31	0.32	0.30	0.30	0.31	0.32	0.31		

TOTALS	100.00	100.00	100.00	100.00	100.00	100.00	100.00	100.00	100.00	100.00	100.00	100.00		
CE	1963-1965													
Unit ID	A4													
Samples	ALGI 12	ALGI 13b	ALGI l4	ALGI 15	ALGI 16	ALGI 17	ALGI 18b	ALGI 19	ALGI 22	ALGI 20	ALGI 21			
Stratigraphy	26	26	26	26	26	26	26	26	26	26	26			
SiO2	54.86	55.62	55.26	54.76	48.63	54.93	54.71	54.97	55.13	55.01	54.33			
Al2O3	16.63	16.90	16.58	16.56	14.68	16.59	16.35	16.25	16.65	16.82	16.31			
CaO	7.83	7.54	7.67	7.84	7.10	7.78	7.97	7.63	7.64	7.74	8.00			
TiO2	0.96	0.97	0.99	1.01	0.90	1.04	1.01	1.05	1.04	1.01	1.02			
K2O	2.02	2.19	2.19	2.16	1.89	2.22	2.14	2.24	2.24	2.19	2.10			
MnO	0.12	2.19	0.12	0.12	10.83	0.12	0.12	0.12	0.12	0.12	0.12			
Fe2O3	8.45	8.25	8.61	8.64	7.81	8.56	8.69	8.95	8.66	8.46	8.92			
Na2O	2.96	3.03	2.91	2.93	2.59	2.91	2.88	2.92	2.99	3.06	2.87			
MgO	5.84	5.04	5.32	5.62	5.26	5.47	5.75	5.47	5.15	5.22	5.93			
P2O5	0.32	2.19	0.36	0.37	0.32	0.38	0.38	0.39	0.38	0.37	0.38			
TOTALS	100.00	2.19	100.00	100.00	100.00	100.00	100.00	100.00	100.00	100.00	100.00			
CE	1963-19635													
Unit ID	A4													
Samples	63A8	63B	63C	63D	63E	63F	63G	63A8	63B	63C	63D	63E	63F	63G
Stratigraphy	26	26	26	26	26	26	26	26	26	26	26	26	26	26
SiO2	55.35	55.32	55.13	55.93	55.35	55.53	55.29	55.35	55.32	55.13	55.93	55.35	55.53	55.29

Al2O3	16.49	16.01	15.94	16.30	16.01	16.07	15.89	16.49	16.01	15.94	16.30	16.01	16.07	15.89
CaO	8.16	8.04	8.14	8.00	8.23	7.84	8.00	8.16	8.04	8.14	8.00	8.23	7.84	8.00
TiO2	0.94	0.95	0.96	0.93	0.94	0.94	0.97	0.94	0.95	0.96	0.93	0.94	0.94	0.97
K2O	1.98	1.97	1.96	2.07	1.95	2.02	2.05	1.98	1.97	1.96	2.07	1.95	2.02	2.05
MnO	0.12	0.12	0.12	0.12	0.12	0.12	0.12	0.12	0.12	0.12	0.12	0.12	0.12	0.12
Fe2O3	7.61	7.86	7.86	7.44	7.75	7.72	7.90	7.61	7.86	7.86	7.44	7.75	7.72	7.90
Na2O	3.33	3.28	3.25	3.34	3.27	3.32	3.24	3.33	3.28	3.25	3.34	3.27	3.32	3.24
MgO	5.71	6.13	6.29	5.51	6.02	6.11	6.20	5.71	6.13	6.29	5.51	6.02	6.11	6.20
P2O5	0.31	0.31	0.35	0.35	0.35	0.33	0.33	0.31	0.31	0.35	0.35	0.35	0.33	0.33
TOTALS	100.00	100.00	100.00	100.00	100.00	100.00	100.00	100.00	100.00	100.00	100.00	100.00	100.00	100.00

Appendix D: Major, minor, and trace elements of 1963-1965 tephras published in Clark et. al. 2006.

CE	1963-1965							
Unit ID	1963-1965							
Samples	8	16	20	21	22B	22D	22L	25
Stratigraphy	26	26	26	26	26	26	26	26
SiO2	53.76	53.66	53.79	54.28	54.91	54.64	53.78	54.42
Al2O3	17.39	17.58	17.60	17.19	16.88	16.78	17.04	17.15
CaO	8.73	8.76	8.52	8.15	8.17	8.33	8.75	8.12
TiO2	1.17	1.14	1.13	1.09	1.10	1.08	0.97	1.13
K2O	2.14	2.18	2.25	2.39	2.33	2.33	2.03	2.24
MnO	0.14	0.13	0.13	0.13	0.13	0.14	0.14	0.13
Fe2O3	8.20	8.02	8.01	7.87	7.83	7.77	8.34	7.90
Na2O	3.31	3.37	3.41	3.43	3.38	3.44	3.23	3.44
MgO	4.70	4.71	4.71	5.06	4.86	5.07	5.36	5.03
P2O5	0.45	0.45	0.45	0.41	0.41	0.42	0.37	0.44
TOTALS	100.00	100.00	100.00	100.00	100.00	100.00	100.00	100.00
Sc	23.20	23.17	22.92	22.82	23.25	23.79	23.84	22.82
V	227.10	224.40	222.80	204.50	216.70	201.00	196.30	206.20
Cr	76.50	76.90	78.90	113.90	98.00	106.70	129.70	101.80
Mn								
Co	26.24	25.94	26.06	25.16	25.65	25.41	26.35	25.55
Cu	116.00	116.00	120.80	109.20	103.80	101.00	103.80	124.90
Zn	77.00	77.20	78.30	75.40	77.20	76.40	71.60	79.70
Ga	14.52	14.64	14.76	14.01	14.13	13.97	14.48	14.63
As								
Rb	57.70	58.70	61.40	67.10	65.50	65.00	56.00	61.20
Sr	818.00	820.30	829.80	759.60	777.50	762.50	827.90	774.20
Y	26.80	26.60	26.90	25.50	26.10	25.40	23.40	25.10
Zr	230.80	231.40	240.20	247.00	241.90	233.50	210.70	237.30

Nb	23.60	23.30	23.70	23.60	23.70	23.40	20.70	24.40
Mo								
Sn								
Cs	0.71	0.73	0.78	0.89	0.85	0.85	0.75	0.82
Ba	875.20	875.20	898.50	886.10	891.00	876.10	811.50	855.10
La	49.24	48.77	49.25	47.38	48.37	47.89	43.18	47.16
Ce	100.80	99.90	100.10	96.20	98.40	97.40	88.30	95.90
Nd	45.17	44.62	44.36	42.03	43.29	42.88	38.95	42.01
Sm	7.93	7.87	7.76	7.31	7.54	7.52	6.86	7.37
Eu	2.14	2.11	2.08	1.91	1.98	1.96	1.87	1.90
Gd	6.55	6.47	6.40	6.06	6.23	6.19	5.66	6.09
Dy	5.05	5.01	4.96	4.72	4.82	4.78	4.41	4.70
Ho	0.93	0.92	0.91	0.87	0.88	0.88	0.81	0.85
Er	2.51	2.49	2.48	2.40	2.39	2.38	2.17	2.32
Yb	2.26	2.25	2.26	2.25	2.18	2.15	1.97	2.12
Lu	0.35	0.35	0.35	0.35	0.34	0.34	0.31	0.33
Hf	5.24	5.26	5.39	5.69	5.46	5.38	4.79	5.41
Ta	1.21	1.22	1.25	1.28	1.27	1.25	1.11	1.31
Pb	5.74	5.73	5.86	6.09	5.86	5.88	5.47	5.81
Th	9.56	9.78	10.28	11.46	11.00	10.96	9.65	10.45
U	3.36	3.44	3.61	4.11	3.88	3.88	3.42	3.70